Comput. Methods Appl. Mech. Engrg. 198 (2008) 194–209

Contents lists available at ScienceDirect

Comput. Methods Appl. Mech. Engrg.

journal homepage: www.elsevier.com/locate/cma

A spacetime discontinuous Galerkin method for hyperbolic heat conduction

S.T. Miller, R.B. Haber *

Department of Mechanical Science and Engineering, University of Illinois at Urbana-Champaign, 1206 W. Green Street, Urbana, IL 61801-2906, USA

ARTICLE INFO

Article history:
Received 5 December 2007
Received in revised form 17 July 2008
Accepted 17 July 2008
Available online 12 August 2008

Keywords:
Hyperbolic heat conduction
Discontinuous Galerkin
Finite element
Shock capturing
Adaptive analysis

ABSTRACT

Non-Fourier conduction models remedy the paradox of infinite signal speed in the traditional parabolic heat equation. For applications involving very short length or time scales, hyperbolic conduction models better represent the physical thermal transport processes. This paper reviews the Maxwell–Cattaneo–Vernotte modification of the Fourier conduction law and describes its implementation within a spacetime discontinuous Galerkin (SDG) finite element method that admits jumps in the primary variables across element boundaries with arbitrary orientation in space and time. A causal, advancing-front meshing procedure enables a patch-wise solution procedure with linear complexity in the number of spacetime elements. An *h*-adaptive scheme and a special SDG shock-capturing operator accurately resolve sharp solution features in both space and time. Numerical results for one spatial dimension demonstrate the convergence properties of the SDG method as well as the effectiveness of the shock-capturing method. Simulations in two spatial dimensions demonstrate the proposed method's ability to accurately resolve continuous and discontinuous thermal waves in problems where rapid and localized heating of the conducting medium takes place.

© 2008 Elsevier B.V. All rights reserved.

1. Introduction

1.1. Hyperbolic heat conduction

The local form of the energy balance equation for purely thermal response is

$$C\dot{T} + \nabla \cdot \mathbf{q} = Q \tag{1}$$

in which $C := \rho c_p$ is the volumetric heat capacity where ρ is the mass density and c_p is the specific heat capacity (measured per unit mass at constant pressure), T is the temperature field, $\mathbf{q}$ is the spatial heat flux vector field, and Q is the volumetric heat supply. The Fourier heat law, $\mathbf{q} = -\boldsymbol{\kappa}\nabla T$ where $\boldsymbol{\kappa}$ denotes the thermal conductivity tensor,[1] is one of the most widely used and accepted constitutive equations of continuum physics. It has held up to almost 200 years of experimental validation remarkably well. Fourier's law gives rise to the familiar parabolic heat equation. However, a parabolic governing equation is paradoxical in the sense that information propagates with infinite signal speeds [1–3]. Although this is a physical impossibility, the parabolic conduction model yields good agreement with experimental data at most length and time scales of engineering and scientific interest. However, at very small time and/or length scales and in certain temperature regimes, predictions based on the Fourier law do not agree well with experimental observations.

Wave-like thermal response with finite propagation speed was first observed experimentally in solid He^4 by Ackerman et al. [4]. Jackson et al. [5] verified this so-called *second sound* phenomenon in high-purity dielectric crystals of sodium fluoride. Narayanamurti and Dynes [6] discovered second sound heat propagation in semimetal bismuth.

While current trends in nanoscale devices and manufacturing processes have sparked renewed interest in hyperbolic conduction laws that deliver finite propagation speeds, the idea is not a new one. A thermal wave model was first proposed by Maxwell [7] in 1867, while Cattaneo [8,9], and Vernotte [10] independently proposed related models in the middle of the last century. Maxwell advocated neglecting the leading term that leads to hyperbolicity, as "... the rate of conduction will rapidly establish itself." However, Cattaneo and Vernotte introduce an additional material parameter, the thermal relaxation time τ, to generate a modification of Fourier's Law:

$$\tau\dot{\mathbf{q}} + \mathbf{q} = -\boldsymbol{\kappa}\nabla T. \tag{2}$$

Various authors refer to (2) as either the Maxwell–Cattaneo, the Cattaneo, the Vernotte, or the Cattaneo–Vernotte equation. For the remainder of this paper, (2) shall be referred to as the MCV equation. For a historical development of the MCV equation, as well as both physical and mathematical justifications for it, see the review articles by Joseph and Preziosi [2,3], Dreyer and Struchtrup

* Corresponding author.
E-mail addresses: smiller5@illinois.edu (S.T. Miller), r-haber@illinois.edu (R.B. Haber).

[1] We assume time-independent thermal parameters in this work for simplicity, but without loss of generality.

0045-7825/$ - see front matter © 2008 Elsevier B.V. All rights reserved.
doi:10.1016/j.cma.2008.07.016

[11], Özisik and Tzou [12], Chandrasekharaiah [13,14], and the references therein. In order to cast the constitutive relation in the format of a conservation law, we use in this work the inverse MCV equation,

$$\boldsymbol{\lambda}(\tau\dot{\mathbf{q}} + \mathbf{q}) = -\nabla T, \tag{3}$$

where $\boldsymbol{\lambda} := \boldsymbol{\kappa}^{-1}$ is the thermal resistivity tensor. Eqs. (1) and (2) can either be solved as a system or, given second-order differentiability for both T and $\mathbf{q}$ and spatial uniformity of τ, be combined into a single wave equation with a damping term:

$$\ddot{T} + \frac{1}{\tau}\dot{T} - \frac{1}{\tau C}\nabla \cdot \boldsymbol{\kappa}(\nabla T) = \frac{1}{\tau C}(Q + \tau\dot{Q}). \tag{4}$$

In either case, the maximum thermal wavespeed, $c = \sqrt{\Lambda/\tau C}$ where Λ is the maximum eigenvalue of $\boldsymbol{\kappa}$, is finite for $\tau > 0$ and realistic material properties. In addition to removing the paradox of infinite signal speed, the hyperbolic thermal model (4) with appropriate initial and boundary conditions yields a well-posed Cauchy problem for the temperature [15].

1.2. Review of numerical methods for the MCV equation

Several variants of the finite difference method have been applied to the hyperbolic thermal problem. Glass et al. [16,17] use MacCormack's scheme; their method provides stability and good resolution at sharp wavefronts, but has the drawback of admitting some oscillations. More recently, Liu et al. [18] use a flux-splitting method to study the transient temperature response due to laser-pulse heating. After splitting the flux, they invoke backward and forward difference schemes to complete the method.

Zhang and Zhao treat problems in one, two, and three spatial dimensions in a series of technical reports [19–21]. For the one-dimensional case, they use a fourth-order compact finite difference scheme with a Crank–Nicolson integrator. A second-order difference scheme with iterative solver is proposed for the two-dimensional solution. The last report presents a second order in time and space difference method with an iterative solver. In all cases, they prove unconditional stability and present studies of numerical error.

Yang [22,23] and later Shen and Han [24,25] proposed total variation diminishing (TVD) schemes. Yang [22] uses a characteristics-based TVD scheme for one-dimensional problems. In [23], the method is extended to two dimensions using a fractional step method. Shen and Han [24,25] apply characteristics-based TVD schemes to problems with complex geometries and boundary conditions in two dimensions. They also note that a dimension-splitting scheme must be used to treat reflections at boundaries. As is the case with other high-order methods, TVD schemes introduce significant diffusion at sharp wavefronts and discontinuities, thereby reducing the accuracy of the solution to first order.[2]

Chen and Lin apply a hybrid numerical technique to problems in one [28] and two [29] spatial dimensions. They first use Laplace transforms to eliminate the temporal dependence, and then use a control volume method to solve the resulting problem. A numerical inversion of the Laplace transform is the final step in their algorithm. The goal of their work is to suppress spurious oscillations in the numerical solution that can appear with other numerical methods. One drawback is that their method can develop instabilities unless suitable parameters are chosen.

Carey and Tsai [30] present the first application of the conforming finite element method (FEM) to the MCV equation. They employ a standard Galerkin weighted residual formulation in space and study the effects of various time integrators. Manzari and Manzari [31,32] propose a mixed finite element scheme for hyperbolic heat conduction. They use a Galerkin weighted residual FEM for spatial discretization and a one-parameter β-method for time integration. The mixed formulation accommodates independent interpolation functions for the temperature and heat flux fields. Xu et al. [33] consider nonlinear material properties and their effects on hyperbolic heat conduction. They discretize the equations using a Bubnov-Galerkin FEM in space and implement a forward difference scheme for time integration. They use an unstructured mesh to investigate temperature-dependent absorptivity during laser heating of a thin film and substrate.

Discontinuous Galerkin (DG) finite element methods have only recently been applied to the MCV equation. Ai and Li [34,35] propose a DG method that permits discontinuities in space only, with an explicit conditionally stable time integrator. They report numerical results obtained with unstructured meshes in three dimensions. Wu and Li [36] present a time-discontinuous Galerkin method that extends earlier work by Li et al. [37]. They discretize space and time simultaneously using a P3–P1 interpolation scheme and weakly enforce continuity of the temperature field across constant-time boundaries. Several authors have proposed DG methods for parabolic diffusion equations, including the classical heat equation. Here we mention a few examples for readers with a more general interest in the DG method for problems with diffusion. Jamet first introduces the DG method for parabolic problems in [38]. Eriksson, Johnson and Larsson published a series of papers on adaptive finite elements for parabolic problems, including [39]; additional citations can be found therein. Zhang and Shu [40] present an analysis of three different DG formulations for diffusion equations. In [41], Zienkiewicz et al. summarize methods in which both advection and diffusion terms are present. Kulkarni et al. propose a DG method for non-conforming meshes in [42]. Chrysafinos and Walkington [43] provide error estimates for the spatially discontinuous Galerkin method for general parabolic problems while allowing for changes in the basis functions between time steps.

1.3. Scope and organization

In this paper, we introduce a spacetime discontinuous Galerkin (SDG) finite element method for the MCV equation. In contrast to methods that support solutions with discontinuities in either space or time (but not both), the SDG method admits discontinuities across any spacetime element boundary without restriction on orientation. We begin with continuum forms of the MCV and energy balance equations, including the jump parts of the differential operators to account for possibly discontinuous solution fields. Then we use a Bubnov-Galerkin weighted residual method to derive a discrete weak form of the problem. The resulting method provides balance (to within machine precision) of the conservation variables at both the element and global levels. As with other discontinuous Galerkin schemes and in contrast to finite volume and finite difference methods, the compact support of SDG basis functions supports high-order schemes without expanding the stencil. The basic SDG formulation is unconditionally stable, although it produces some overshoot and undershoot in the vicinity of solution discontinuities. These artifacts, when they occur, remain local and do not pollute the global solution. In applications where this overshoot is undesirable, we apply a special SDG shock-capturing operator [44] that derives from the sub-cell method proposed by Persson and Peraire [45].

Our SDG method employs an advancing-front meshing/solution procedure that generates unstructured spacetime meshes that obey a special *causality constraint* based on the characteristics of the governing partial differential equations [46–48] (see also Section 4.1). The causality constraint imposes a local restriction on

[2] Goodman and LeVeque [26] prove that TVD schemes in 2D are at most first-order accurate. LeVeque [27] further states that combining a high-order 1D scheme with flux splitting in 2D can produce higher-order accurate results in smooth regions.

mesh advancement in time, but there are no global restrictions. Thus, regions of the mesh where the elements have small spatial diameters do not limit time advancement in regions where the elements have large spatial diameters. We exploit this flexibility in an *h*-adaptive analysis method that simultaneously adjusts spatial and temporal element diameters to achieve significant performance gains. This highly dynamic adaptive scheme is particularly effective in resolving the sharp wavefronts that can arise in hyperbolic thermal solutions. The causality constraint implies that the local solution on each new patch of elements produced by the spacetime mesh generator depends exclusively on prescribed initial and boundary data and on data from previously solved patches; it is decoupled from the solutions on all subsequent elements. This decoupling enables a scalable patch-by-patch solution procedure with $\mathcal{O}(N)$ computational complexity, where N is the number of spacetime elements, that interleaves patch generation with local, patch-wise finite element solutions. The organization of the remainder of this paper is as follows. Section 2 presents the continuum formulation of the MCV thermal problem. In Section 2.1, we review useful concepts from the exterior calculus on spacetime manifolds and introduce a notation for differential forms with vector coefficients. We develop the continuum governing equations in Section 2.2 by localizing the integral forms of the energy and MCV equations. Section 3 formulates the SDG method; a Bubnov-Galerkin weighted residual statement for a single spacetime element leads to the discrete weak form that defines the SDG method. We introduce a shock-capturing method for our SDG method in Section 3.3. Section 4 describes an implementation of the SDG method and details our advancing-front meshing procedure. Numerical results appearing in Section 5 include: convergence studies and a demonstration of the shock-capturing operator in one spatial dimension, an example involving pulsed-laser heating of a thin film and examples involving material microstructures with voids or inclusions subjected to discontinuous thermal loading. Conclusions and directions for future research are discussed in Section 6. Lastly, the appendices present component expansions of the discrete weak statement and expressions for the Riemann values that determine the flux jump conditions.

2. Continuum formulation

2.1. Differential forms notation for spacetime manifolds

We use the notation of differential forms on spacetime manifolds to develop the SDG formulation. This approach supports a direct, coordinate-free notation and leads to concise representations of the governing equations that emphasize the notion of conservation over spacetime control volumes. It also circumvents a fundamental problem that arises with conventional tensor notation in spacetime versions of the Stokes Theorem, where the absence (in non-relativistic settings) of an inner product for spacetime vectors leaves the notion of a "unit normal vector" ill-defined. In this subsection, we present definitions and notations for differential forms with vector coefficients on spacetime manifolds. See [49,50] for a more complete exposition of differential forms and the exterior calculus on manifolds. Our formulation is specialized to flat spacetimes for simplicity.

Consider a flat spacetime manifold $\mathscr{D} \subset \mathscr{M} := \mathbb{E}^d \times \mathbb{R}$ in which d is the spatial dimension of the manifold. We use the basis $\{\mathbf{e}_i, \mathbf{e}_t\}_{i=1}^d$, in which the spatial basis $\{\mathbf{e}_i\}$ spans $\mathbb{E}^d$ and $\mathbf{e}_t$ is the temporal basis for $\mathbb{R}$, to represent vectors in the tangent space $\mathscr{T}$. The tangent bundle for our flat spacetime is uniform over $\mathscr{M}$, so we denote the tangent space at all points $P \in \mathscr{M}$ simply as $\mathscr{T}$, rather than the usual $\mathscr{T}_P$. The dual basis for covectors in $\mathscr{T}^*$ is denoted as $\{\boldsymbol{e}^i, \boldsymbol{e}^t\}_{i=1}^d$ and is determined by the relations $\boldsymbol{e}^i(\mathbf{e}_j) = \delta^i_j$, $\boldsymbol{e}^i(\mathbf{e}_t) = 0$, $\boldsymbol{e}^t(\mathbf{e}_i) = 0$ and $\boldsymbol{e}^t(\mathbf{e}_t) = 1$. Thus, the component representations of any vector $\mathbf{a} \in \mathscr{T}$ and any covector $\boldsymbol{b} \in \mathscr{T}^*$ are $\mathbf{a} = a^i\mathbf{e}_i + a^t\mathbf{e}_t$ and $\boldsymbol{b} = b_i\boldsymbol{e}^i + b_t\boldsymbol{e}^t$ in which, and from here on, summation from 1 to d is implied for indices repeated between subscripts and superscripts, excepting the reserved index t for which no summation is implied.

Let $\mathscr{T}^r := \mathscr{T} \times \cdots \times \mathscr{T}$ (r times) be the space of r-vectors; the space of r-covectors (*i.e.*, alternating, r-linear functions on $\mathscr{T}^r$) is denoted by $\Lambda^r\mathscr{T}^*$. The standard basis for r-covectors is denoted by $\{\boldsymbol{e}^\lambda\}$, in which $\lambda = i_1, \ldots, i_r$ is a strictly increasing r-index. Any r-covector $\omega \in \Lambda^r\mathscr{T}^*$ has a unique component representation with respect to the standard basis, $\boldsymbol{\omega} = \omega_\lambda \boldsymbol{e}^\lambda$, in which summation over strictly increasing r-indices is implied. We use "$\wedge$" to denote the usual exterior product operator and $\mathbf{d}$ to denote the exterior derivative (*cf.* [49]).

A differential r-form on $\mathscr{D}$ (with scalar coefficients) is an r-covector field on $\mathscr{D}$; we call these *r-forms* for short. The standard basis for 1-forms is $\{\mathrm{d}x^i, \mathrm{d}t\}_{i=1}^d$, where for our flat manifold the $\mathrm{d}x^i$ are 1-forms with uniform values $\boldsymbol{e}^i$, and $\mathrm{d}t$ is the 1-form with uniform value $\boldsymbol{e}^t$. Thus, any 1-form with scalar coefficients has the unique component representation with respect to the standard basis, $\boldsymbol{\omega} = \omega_i \mathrm{d}x^i + \omega_t \mathrm{d}t$, in which ω_i and ω_t are scalar fields on $\mathscr{D}$. Top forms in spacetime are $(d+1)$-forms, for which the standard basis is the singleton set $\{\boldsymbol{\Omega}\}$, where $\boldsymbol{\Omega} = \mathrm{d}x^1 \wedge \ldots \wedge \mathrm{d}x^d \wedge \mathrm{d}t$. Thus, a top-form $\boldsymbol{\alpha}$ with scalar coefficients is expressed as $\boldsymbol{\alpha} = \alpha\boldsymbol{\Omega}$ in which α is a scalar function on $\mathscr{D}$. Our formulation makes use of forms with both scalar and vector coefficients. The usual definition of the exterior product operator addresses forms with scalar coefficients; here we extend the definition to address forms with vector coefficients. Let $\boldsymbol{\alpha}$ and $\boldsymbol{\beta}$ be r- and s-forms on $\mathscr{D}$, respectively, let $\mathbf{a}$ and $\mathbf{b}$ be vector fields on $\mathscr{D}$, and let w be a scalar field on $\mathscr{D}$. We write $\mathbf{a}\boldsymbol{\alpha}$ and $\mathbf{b}\boldsymbol{\beta}$ to describe an r-form and an s-form with vector coefficients. The exterior product of $\mathbf{a}\boldsymbol{\alpha}$ and $\mathbf{b}\boldsymbol{\beta}$ is the $(r+s)$-form with scalar coefficients given by

$$\mathbf{a}\boldsymbol{\alpha} \wedge \mathbf{b}\boldsymbol{\beta} := \mathbf{a} \cdot \mathbf{b}(\boldsymbol{\alpha} \wedge \boldsymbol{\beta}). \tag{5}$$

A magnitude operator for forms with scalar or vector coefficients is defined by

$$|w\boldsymbol{\alpha}| := |w|\boldsymbol{\alpha} \quad |\mathbf{a}\boldsymbol{\alpha}| := |\mathbf{a}|\boldsymbol{\alpha}. \tag{6}$$

Let $\boldsymbol{\alpha}$ be an r-form with $r \in \{x \in \mathbb{N} : x \leqslant d+1\}$. The Hodge star operator, denoted as $\bigstar$, is defined by $\boldsymbol{\alpha} \wedge \bigstar\boldsymbol{\alpha} = \boldsymbol{\Omega}$, in which $\bigstar\boldsymbol{\alpha}$ is a $(d+1-r)$-form. We shall have use of d-forms, for which we define a preferred basis $\{\bigstar \mathrm{d}x^i, \bigstar \mathrm{d}t\}_{i=1}^d$. This implies $\mathrm{d}x^i \wedge \bigstar \mathrm{d}x^k = \delta^{ik}\boldsymbol{\Omega}$, $\mathrm{d}t \wedge \bigstar \mathrm{d}x^j = \boldsymbol{0}$ and $\mathrm{d}x^j \wedge \bigstar \mathrm{d}t = \boldsymbol{0}$ for $j, k = 1, \ldots, d$. We define the action of the Hodge star operator on a form with vector coefficients as $\bigstar(\mathbf{a}\boldsymbol{\alpha}) = \mathbf{a}\bigstar\boldsymbol{\alpha}$, where $\mathbf{a}$ and $\boldsymbol{\alpha}$ are a vector field and an r-form, respectively, on $\mathscr{D}$.

We introduce a useful 1-form with vector coefficients and an associated d-form with vector coefficients to facilitate our formulation:

$$\mathbf{dx} := \mathbf{e}_i \mathrm{d}x^i \quad \bigstar\mathbf{dx} := \mathbf{e}_i \bigstar \mathrm{d}x^i. \tag{7}$$

Given any differentiable scalar field w on $\mathscr{D}$, we find

$$\mathbf{d}(w\bigstar\mathbf{dx}) = (\nabla w)\boldsymbol{\Omega} \quad \mathbf{d}(w\bigstar\mathrm{d}t) = \dot{w}\boldsymbol{\Omega}. \tag{8}$$

For any differentiable vector field $\mathbf{a}$ on $\mathscr{D}$, we have

$$\mathbf{d}(\mathbf{a} \wedge \bigstar\mathbf{dx}) = (\boldsymbol{\nabla} \cdot \mathbf{a})\boldsymbol{\Omega} \quad \mathbf{d}(\mathbf{a} \wedge \bigstar\mathrm{d}t) = \dot{\mathbf{a}}\boldsymbol{\Omega}. \tag{9}$$

Let $\{\boldsymbol{\alpha}_i\}_{i=1}^n$ and $\{\boldsymbol{\beta}_i\}_{i=1}^n$ be n-tuples of differential forms. To facilitate our treatment of systems, we extend the exterior derivative, exterior product, Hodge star and magnitude operators to act on n-tuples of forms as follows.

$$\mathbf{d}\begin{Bmatrix}\alpha_1\\ \vdots\\ \alpha_n\end{Bmatrix}=\begin{Bmatrix}\mathbf{d}\alpha_1\\ \vdots\\ \mathbf{d}\alpha_n\end{Bmatrix}\quad \begin{Bmatrix}\alpha_1\\ \vdots\\ \alpha_n\end{Bmatrix}\wedge\begin{Bmatrix}\beta_1\\ \vdots\\ \beta_n\end{Bmatrix}=\begin{Bmatrix}\alpha_1\wedge\beta_1\\ \vdots\\ \alpha_n\wedge\beta_n\end{Bmatrix}$$
$$\star\begin{Bmatrix}\alpha_1\\ \vdots\\ \alpha_n\end{Bmatrix}=\begin{Bmatrix}\star\alpha_1\\ \vdots\\ \star\alpha_n\end{Bmatrix}\qquad \left|\begin{Bmatrix}\alpha_1\\ \vdots\\ \alpha_n\end{Bmatrix}\right|=\begin{Bmatrix}|\alpha_1|\\ \vdots\\ |\alpha_n|\end{Bmatrix} \tag{10}$$

Consider any open region $\mathscr{Q}\subset\mathscr{D}$ with a regular boundary $\partial\mathscr{Q}$. We write the Stokes Theorem in differential forms notation as [49]

$$\int_{\mathscr{Q}}\mathbf{d}\omega=\int_{\partial\mathscr{Q}}\omega \tag{11}$$

in which ω is a d-form with either scalar or vector coefficients.

2.2. Governing equations

This section presents the governing system of equations for energy balance and the MCV constitutive law using differential forms notation, emphasizing their common structure as conservation laws with source terms. We begin with the integral form of the system and apply the Stokes Theorem (11) to derive the localized governing equations. Since the hyperbolic system supports discontinuous solutions, we address both the diffuse and jump parts of the localized equations. The conservation laws format allows us to adopt the SDG method proposed in [51] to discretize the problem.

Let $\mathscr{D}\subset\mathscr{M}$ be the $(d+1)$-dimensional spacetime analysis domain, where $\mathscr{D}$ has a suitably regular boundary $\partial\mathscr{D}$, as shown in Fig. 1. We introduce a 2-tuple of conservation fields,

$$\mathbf{u}=\begin{Bmatrix}\mathbf{u}_1\\ \mathbf{u}_2\end{Bmatrix}=\begin{Bmatrix}e\\ \boldsymbol{\eta}\end{Bmatrix}, \tag{12}$$

where we define $e:=CT$ and $\boldsymbol{\eta}:=\boldsymbol{\lambda}(\tau\mathbf{q})$. The material parameters $C,\boldsymbol{\lambda}$ and τ are assumed to be known, time-independent functions of position $\mathbf{x}$. Next, consider the 2-tuples of spacetime fluxes and spacetime sources,

$$\mathbf{F}=\begin{Bmatrix}\boldsymbol{F}_e(\mathbf{u},\mathbf{x},t)\\ \boldsymbol{F}_\eta(\mathbf{u},\mathbf{x},t)\end{Bmatrix}\quad \mathbf{S}=\begin{Bmatrix}\boldsymbol{S}_e(\mathbf{u},\mathbf{x},t)\\ \boldsymbol{S}_\eta(\mathbf{u},\mathbf{x},t)\end{Bmatrix} \tag{13}$$

in which a subscript 'e' denotes a quantity related to thermal energy balance (1) and a subscript 'η' denotes a quantity related to the inverse MCV equation (3). The spacetime fluxes, $\boldsymbol{F}_e$ and $\boldsymbol{F}_\eta$, are d-forms whose restrictions to any spacetime d-manifold embedded in $\mathscr{D}$ deliver the fluxes of the associated quantities (*i.e.*, thermal energy or the quantity $\boldsymbol{\lambda}(\tau\mathbf{q})$) across the d-manifold. In particular, we have

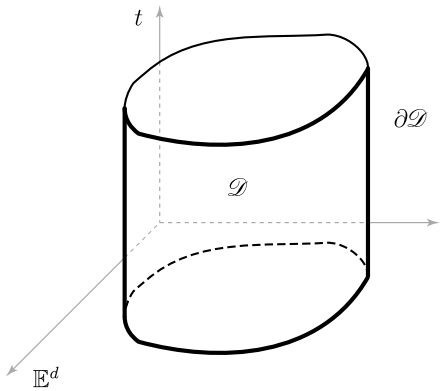

Fig. 1. Spacetime analysis domain $\mathscr{D}$ with boundary $\partial\mathscr{D}$ in $\mathbb{E}^d\times\mathbb{R}$.

$$\boldsymbol{F}_e=CT\star\mathrm{d}t+\mathbf{q}\wedge\star\mathbf{dx}\quad \boldsymbol{F}_\eta=\boldsymbol{\lambda}(\tau\mathbf{q})\star\mathrm{d}t+T\star\mathbf{dx} \tag{14}$$

and the source terms,

$$\boldsymbol{S}_e=-Q\boldsymbol{\Omega}\quad \boldsymbol{S}_\eta=\boldsymbol{\lambda}(\mathbf{q})\boldsymbol{\Omega} \tag{15}$$

in which $Q:\mathscr{D}\to\mathbb{R}$. The integral form of the system of conservation laws is then written as,

$$\int_{\partial\mathscr{Q}}\mathbf{F}+\int_{\mathscr{Q}}\mathbf{S}=\mathbf{0}\quad\forall\mathscr{Q}\subset\mathscr{D} \tag{16}$$

in which only open subdomains $\mathscr{Q}$ with suitably regular boundaries are considered.

We apply the Stokes Theorem and the Localization Theorem to obtain the system of governing equations on each $\mathscr{Q}\subset\mathscr{D}$,

$$(\mathbf{dF}+\mathbf{S})|_{\mathscr{Q}}=\mathbf{0}, \tag{17a}$$
$$(\mathbf{F}^*-\mathbf{F})|_{\partial\mathscr{Q}}=\mathbf{0} \tag{17b}$$

in which $\mathbf{F}^*$ is a 2-tuple containing target fluxes $\boldsymbol{F}_e^*$ and $\boldsymbol{F}_\eta^*$ on $\partial\mathscr{Q}$, and $\mathbf{F}|_{\partial\mathscr{Q}}$ (without decoration) denotes the interior trace of $\mathbf{F}$ on $\partial\mathscr{Q}$. The target fluxes derive from Riemann values on portions of $\partial\mathscr{Q}$ on the interior of $\mathscr{D}$ and from initial/boundary conditions on $\partial\mathscr{Q}\cap\partial\mathscr{D}$, as explained below. The term $\mathbf{dF}$ in (17a) represents the diffuse part of the exterior derivative operator, while (17b) is the jump part that accounts for possible discontinuities in the solution fields. Expanding (17a) with the aid of (8) and (9) yields the system,

$$\begin{Bmatrix}C\dot{T}+\boldsymbol{\nabla}\cdot\mathbf{q}-Q\\ \boldsymbol{\lambda}(\tau\dot{\mathbf{q}}+\mathbf{q})+\nabla T\end{Bmatrix}\boldsymbol{\Omega}=\begin{Bmatrix}0\\ \mathbf{0}\end{Bmatrix}\boldsymbol{\Omega}, \tag{18}$$

that contains the residual forms of (1) and (3).

We follow the method of [51] in expressing the jump condition (17b) with respect to target values that depend on the interior and exterior traces of the fluxes as well as the local orientation of $\partial\mathscr{Q}$. This is a more stringent condition than the usual form of the jump condition, but it maintains the correct characteristic structure across singular surfaces and has been shown (for scalar conservation laws) to guarantee satisfaction of the entropy condition in the weak formulation and to reduce numerical dissipation [51]. In the case of linear conservation laws, such as those considered here, explicit expressions for the Riemann values are available that are reasonably inexpensive to compute. Thus, there is no need to consider numerical fluxes based on approximate Riemann solvers.

2.3. Boundary partitions and computation of target fluxes $\mathbf{F}^*$

The values of $\mathbf{F}^*$ in (17b) depend on the local orientation of $\partial\mathscr{Q}$. We consider only hyperbolic problems with well-defined characteristic directions, and use the notion of causality to develop a disjoint partition of $\partial\mathscr{Q}$ into open subsets $\partial\mathscr{Q}^{\mathrm{ci}}$, $\partial\mathscr{Q}^{\mathrm{co}}$ and $\partial\mathscr{Q}^{\mathrm{nc}}$ such that $\partial\mathscr{Q}=\overline{\partial\mathscr{Q}^{\mathrm{ci}}\cup\partial\mathscr{Q}^{\mathrm{co}}\cup\partial\mathscr{Q}^{\mathrm{nc}}}$. We say that a d-manifold is causal if all characteristics pass through it in the same direction.[3] As depicted in Fig. 2, the causal inflow boundary $\partial\mathscr{Q}^{\mathrm{ci}}$ is the subset of $\partial\mathscr{Q}$ where the characteristic directions all point into the interior of $\mathscr{Q}$. Similarly, the causal outflow boundary $\partial\mathscr{Q}^{\mathrm{co}}$ is the part where all characteristic directions point to the exterior of $\mathscr{Q}$. The non-causal boundary is defined by $\partial\mathscr{Q}^{\mathrm{nc}}:=\partial\mathscr{Q}\setminus\overline{\partial\mathscr{Q}^{\mathrm{ci}}\cup\partial\mathscr{Q}^{\mathrm{co}}}$. That is, the characteristic directions at each location on the non-causal boundary point to both the interior and exterior of $\mathscr{Q}$.

We similarly partition the boundary of the spacetime analysis domain $\mathscr{D}$. Initial conditions are prescribed on the domain causal inflow boundary $\partial\mathscr{D}^{\mathrm{ci}}$, and no conditions are imposed on the domain causal outflow boundary $\partial\mathscr{D}^{\mathrm{co}}$. We apply boundary conditions

[3] 'Causal' has the same meaning as 'spacelike' in the physics literature.

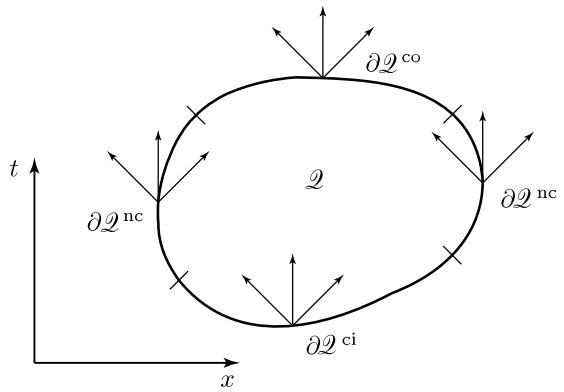

Fig. 2. Depiction of boundary partition for a subdomain $\mathscr{Q} \subset \mathbb{E}^1 \times \mathbb{R}$. Arrows indicate local characteristic directions on $\partial\mathscr{Q}$.

on the domain non-causal boundary $\partial\mathscr{D}^{\mathrm{nc}}$. We further partition the non-causal boundary into disjoint Dirichlet and Neumann parts according to $\overline{\partial\mathscr{D}^{\mathrm{nc}}} = \overline{\partial\mathscr{D}_e^{\mathrm{nc}} \cup \partial\mathscr{D}_\eta^{\mathrm{nc}}}$. Prescribed boundary fluxes corresponding to $\boldsymbol{F}_e(\boldsymbol{F}_\eta)$ are applied on $\partial\mathscr{D}_e^{\mathrm{nc}}(\partial\mathscr{D}_\eta^{\mathrm{nc}})$.

For a regular subdomain $\mathscr{Q} \subset \mathscr{D}$, the target fluxes $\mathbf{F}^*$ on the boundary $\partial\mathscr{Q}$ are given by

$$\boldsymbol{F}_e^*|_{\partial\mathscr{Q}} = \begin{cases} \boldsymbol{F}_e & \text{on } \partial\mathscr{Q}^{\mathrm{co}} \\ \boldsymbol{F}_e^+ & \text{on } \partial\mathscr{Q}^{\mathrm{ci}} \cup (\partial\mathscr{D}_e^{\mathrm{nc}} \cap \partial\mathscr{Q}^{\mathrm{nc}}) \\ \boldsymbol{F}_e^{\mathrm{R}} & \text{on } \partial\mathscr{Q}^{\mathrm{nc}} \setminus \partial\mathscr{D}^{\mathrm{nc}} \end{cases} \tag{19a}$$

$$\boldsymbol{F}_\eta^*|_{\partial\mathscr{Q}} = \begin{cases} \boldsymbol{F}_\eta & \text{on } \partial\mathscr{Q}^{\mathrm{co}} \\ \boldsymbol{F}_\eta^+ & \text{on } \partial\mathscr{Q}^{\mathrm{ci}} \cup (\partial\mathscr{D}_\eta^{\mathrm{nc}} \cap \partial\mathscr{Q}^{\mathrm{nc}}) \\ \boldsymbol{F}_\eta^{\mathrm{R}} & \text{on } \partial\mathscr{Q}^{\mathrm{nc}} \setminus \partial\mathscr{D}^{\mathrm{nc}} \end{cases} \tag{19b}$$

in which the case with no superscript denotes the interior trace, a superscript '+' indicates the exterior trace, and a superscript 'R' denotes a Riemann flux defined by the solution to the local Riemann problem (*cf.* [27]). The exterior traces are obtained from the solution on an adjacent part of the spacetime domain or from prescribed boundary and initial data, as appropriate. Detailed expressions for $\boldsymbol{F}_e^{\mathrm{R}}$ and $\boldsymbol{F}_\eta^{\mathrm{R}}$ appear in the Appendix.

3. SDG formulation

This section introduces a spacetime discontinuous Galerkin finite element method based on a weak form of (17). We first introduce a disjoint partition $\mathscr{P}_h$ of the spacetime analysis domain $\mathscr{D}$ into N open subdomains $\mathscr{Q}_\alpha$, such that $\mathscr{P} = \{\mathscr{Q}_\alpha\}_{\alpha=1}^N$. From here on, we refer to the subdomains as finite elements and to the partition $\mathscr{P}_h$ as the spacetime mesh. Rather than enforce the governing equations (17) on all $\mathscr{Q} \subset \mathscr{D}$, we seek a discrete approximation by weakly enforcing (17) only on each element $\mathscr{Q} \in \mathscr{P}_h$. To this end, we use the mesh $\mathscr{P}_h$ to construct a discrete, discontinuous Galerkin solution space that is piecewise continuous on $\mathscr{D}$ with jumps admissible across element boundaries: $\mathscr{V}_h := \{\mathbf{w} : \omega|_{\mathscr{Q}} \in \mathscr{P}^r_{\mathscr{Q}}; w_i|_{\mathscr{Q}} \in \mathscr{P}^s_{\mathscr{Q}}\ \forall \mathscr{Q} \in \mathscr{P}_h, i = 1,\dots,d\}$, where $\mathscr{P}^k_{\mathscr{Q}}$ is the space of polynomial functions of order k on $\mathscr{Q}$ and r and s are selected non-negative integers. In the numerical examples reported here, we find it convenient to set $r = s$ and to use the same polynomial order in all elements, although either or both of these constraints could be relaxed. The components of the 2-tuple $\mathbf{w} := (\omega, \mathbf{w})^{\mathrm{T}}$ are a scalar and a vector field on $\mathscr{D}$, consistent with the structure of (13), and we use w_i to denote the scalar components of $\mathbf{w}$. We use polynomial basis functions with support on individual elements to construct $\mathscr{V}_h$ and write $\mathscr{V}_h^{\mathscr{Q}} = \mathscr{V}_h|_{\mathscr{Q}}$ for each element $\mathscr{Q} \in \mathscr{P}_h$. The discrete weighted residuals statement follows from the Bubnov-Galerkin version of the Method of Weighted Residuals as applied to (17).

3.1. Discrete weighted residuals statement

For each $\mathscr{Q} \in \mathscr{P}_h$, find $\mathbf{u} \in \mathscr{V}_h^{\mathscr{Q}}$ such that

$$\int_{\mathscr{Q}} \mathbf{w} \wedge (\mathbf{dF} + \mathbf{S}) + \int_{\partial\mathscr{Q}} \mathbf{w} \wedge (\mathbf{F}^* - \mathbf{F}) = \mathbf{0} \quad \forall \mathbf{w} \in \mathscr{V}_h^{\mathscr{Q}}. \tag{20}$$

We apply the Stokes Theorem to (20) to get the discrete weak form.

3.2. Discrete weak form

For each $\mathscr{Q} \in \mathscr{P}_h$, find $\mathbf{u} \in \mathscr{V}_h^{\mathscr{Q}}$ such that

$$\int_{\mathscr{Q}} (-\mathbf{dw} \wedge \mathbf{F} + \mathbf{w} \wedge \mathbf{S}) + \int_{\partial\mathscr{Q}} \mathbf{w} \wedge \mathbf{F}^* = \mathbf{0} \quad \forall \mathbf{w} \in \mathscr{V}_h^{\mathscr{Q}}. \tag{21}$$

We use (13) to expand (21) as

$$\int_{\mathscr{Q}} \left\{ \begin{matrix} -\mathbf{d}\omega \wedge \boldsymbol{F}_e + \omega \boldsymbol{S}_e \\ -\mathbf{dw} \wedge \boldsymbol{F}_\eta + \mathbf{w} \wedge \boldsymbol{S}_\eta \end{matrix} \right\} + \int_{\partial\mathscr{Q}} \left\{ \begin{matrix} \omega \boldsymbol{F}_e^* \\ \mathbf{w} \wedge \boldsymbol{F}_\eta^* \end{matrix} \right\} = \left\{ \begin{matrix} 0 \\ 0 \end{matrix} \right\} \quad \forall (\omega, \mathbf{w})^{\mathrm{T}} \in \mathscr{V}_h^{\mathscr{Q}}. \tag{22}$$

In view of the independence of ω and $\mathbf{w}$, we can also write

$$\int_{\mathscr{Q}} (-\mathbf{d}\omega \wedge \boldsymbol{F}_e + \omega \boldsymbol{S}_e - \mathbf{dw} \wedge \boldsymbol{F}_\eta + \mathbf{w} \wedge \boldsymbol{S}_\eta) + \int_{\partial\mathscr{Q}} (\omega \boldsymbol{F}_e^* + \mathbf{w} \wedge \boldsymbol{F}_\eta^*) = 0 \quad \forall (\omega, \mathbf{w})^{\mathrm{T}} \in \mathscr{V}_h^{\mathscr{Q}}. \tag{23}$$

The Cartesian component expansion of (23) can be found in the Appendix.

3.3. Shock capturing

The SDG formulation (23) is unconditionally stable when applied to systems of linear conservation laws, such as those considered here. However, the basic SDG formulation exhibits local overshoot and undershoot in the vicinity of solution discontinuities, except in the special case of piecewise-constant models. Although the method's element-wise conservation properties prevent these numerical artifacts from polluting the solution globally, there exist applications where it is desirable to suppress them. In this section, we present a shock-capturing scheme that controls overshoot and undershoot. We use the SDG shock-capturing scheme of Palaniappan et al. [44] which derives from the sub-cell method of Persson and Peraire [45]. In this scheme, we add artificial diffusion to the governing equation (17) in those elements where non-smooth response is detected by a discontinuity sensor, as described below. The specific form of the diffusion operator is chosen to preserve the element-wise conservation property of the basic SDG formulation. Let $\mathbf{p}$ denote a 2-tuple of d-forms defined as exterior products of the spatial gradients of the components of $\mathbf{u}$ with $\star\mathbf{dx}$,

$$\mathbf{p} := \left\{ \begin{matrix} \nabla e \wedge \star\mathbf{dx} \\ \nabla \boldsymbol{\eta} \wedge \star\mathbf{dx} \end{matrix} \right\} = \left\{ \begin{matrix} \nabla(CT) \wedge \star\mathbf{dx} \\ \nabla(\boldsymbol{\lambda}(\tau\mathbf{q})) \wedge \star\mathbf{dx} \end{matrix} \right\}, \tag{24}$$

where, in view of the possibility of discontinuous material data and solution fields, $\mathbf{p}$ is defined almost everywhere on $\mathscr{D}$. We augment (17) with an artificial diffusion term to obtain,

$$[\mathbf{d}(\mathbf{F} - \alpha^{\mathscr{Q}}\mathbf{p}) + \mathbf{S}]|_{\mathscr{Q}} = \mathbf{0}, \tag{25a}$$

$$[\mathbf{F}^* - \mathbf{F} - \alpha^{\mathscr{Q}}(\mathbf{p}^* - \mathbf{p})]|_{\partial\mathscr{Q}} = \mathbf{0} \tag{25b}$$

in which $\alpha^{\mathscr{Q}}$ is a uniform diffusivity for element $\mathscr{Q}$, $-\alpha^{\mathscr{Q}}\mathbf{p}$ represents the flux due to artificial diffusion and $\mathbf{p}^*$ is the target value for $\mathbf{p}$. Replacing the residuals in (20) with those given in (25), setting $\mathbf{p}^* = \mathbf{0}$, and applying the Stokes Theorem, we obtain the stabilized weak problem:

For each $\mathscr{Q} \in \mathscr{P}_h$, find $\mathbf{u} \in \mathscr{V}_h^{\mathscr{Q}}$ such that

$$\int_{\mathscr{Q}} [-\mathbf{dw} \wedge (\mathbf{F} - \alpha^{\mathrm{Q}}\mathbf{p}) + \mathbf{w} \wedge \mathbf{S}] + \int_{\partial\mathscr{Q}} \mathbf{w} \wedge \mathbf{F}^* = \mathbf{0} \quad \forall \mathbf{w} \in \mathscr{V}_h^{\mathscr{Q}}. \tag{26}$$

Specifying $\mathbf{p}^* = \mathbf{0}$ preserves the SDG method's element-wise conservation property and maintains the integrity of our patch-by-patch solution procedure, *cf.* [44]. The weak form (26) defines the stabilized SDG method, but it remains to define a shock-capturing scheme for sensing discontinuities and adjusting the strength of the artificial diffusion within each element. Although the intensity of the artificial diffusion can be adjusted on a per-element basis, our numerical experience indicates that it is best to adjust the diffusion on a per-patch basis, as described below.

Let $\{u_{\gamma j}\}_{j=1}^{d(m_\gamma)}$ be the set of scalar components of the conservation field $\mathbf{u}_\gamma$, where $m_1 = 0$ and $m_2 = 1$. We expand the components $u_{\gamma j}$ in each element $\mathscr{Q}$ using a hierarchical polynomial basis. For polynomial degree p, we have $N(p)$ basis functions $\{\psi_i\}_{i=1}^{N(p)}$, and the solution components on $\mathscr{Q}$ are expressed as

$$u_{\gamma j} = \sum_{i=1}^{N(p)} u_{\gamma j}^i \psi_i. \tag{27}$$

A truncation of the solution on $\mathscr{Q}$ to order $(p-1)$ in the hierarchical basis is given by

$$\hat{u}_{\gamma j} = \sum_{i=1}^{N(p-1)} u_{\gamma j}^i \psi_i. \tag{28}$$

We construct $\mathbf{u}_\gamma$ and its truncation $\hat{\mathbf{u}}_\gamma$ using the scalar component fields defined in (27) and (28).

A discontinuity sensor for $\mathbf{u}_\gamma$ in element $\mathscr{Q}$ measures the level of participation of the highest-order basis functions in the solution:

$$\Sigma_\gamma^{\mathscr{Q}} = \frac{\|\mathbf{u}_\gamma - \hat{\mathbf{u}}_\gamma\|_{L_2(\mathscr{Q})}}{\|\mathbf{u}_\gamma\|_{L_2(\mathscr{Q})}}. \tag{29}$$

No stabilization is required for the overly diffusive piecewise-constant case, so we skip the computation in (29) and set $\Sigma_\gamma^{\mathscr{Q}} = 0$ when $p = 0$. To avoid a possible divide by zero when $p > 0$, we first compare $\|\mathbf{u}_\gamma\|_{L_2(\mathscr{Q})}$ to the norm of a reference magnitude for $\mathbf{u}_\gamma$, denoted by u_γ^0, and test for a near-zero solution. If $\|\mathbf{u}_\gamma\|_{L_2(\mathscr{Q})}/(u_\gamma^0|\mathscr{Q}|)$ is found to be near zero on $\mathscr{Q}$, we skip the computation in (29), and set $\Sigma_\gamma^{\mathscr{Q}} = 0$. See [44] for further details.

We expect $\Sigma_\gamma^{\mathscr{Q}}$ to decay with increasing polynomial order according to $1/(p+1)^4$ when the solution is smooth near element $\mathscr{Q}$ [45]; a slower rate of decay indicates the presence of a non-smooth solution feature. Accordingly, we propose the following shock-capturing scheme for adjusting the strength of the artificial diffusion. Let $s_\gamma^{\mathscr{Q}} := \log(\Sigma_\gamma^{\mathscr{Q}})$. The intensity of artificial diffusion for conservation field u_γ in element $\mathscr{Q}$ is

$$\alpha_\gamma^{\mathscr{Q}} = \begin{cases} 0 & \text{if } s_\gamma^{\mathscr{Q}} < \tilde{s} - \beta, \\ \frac{\tilde{\alpha}}{2}\left[1 + \frac{s_\gamma^{\mathscr{Q}} - \tilde{s}}{\beta}\right] & \text{if } \tilde{s} - \beta \leqslant s_\gamma^{\mathscr{Q}} \leqslant \tilde{s} + \beta, \\ \tilde{\alpha} & \text{if } s_\gamma^{\mathscr{Q}} > \tilde{s} + \beta \end{cases} \tag{30}$$

in which $\tilde{\alpha} = C_\alpha c h/p$ and $\tilde{s} = \log[C_s/(p+1)^4]$; here h denotes the spatial diameter of element $\mathscr{Q}$, c is the thermal wave speed (*cf.* 1.1), while C_α, C_s and β are user-selected parameters. The effect of (30) is to eliminate artificial diffusion in elements where the sensor decays somewhat faster than the expected rate, with a linear ramp to the maximum-strength artificial diffusion in elements where the indicator decays more slowly than expected.

In practice, we find it best to use the same diffusion value for all fields and for all elements within each patch. Thus, we determine the element diffusions in patch $\mathbb{P}$ according to

$$\alpha^{\mathscr{Q}} = \alpha^{\mathbb{P}} := \max_{\bar{\mathscr{Q}} \in \mathbb{P}} \left(\max_{\gamma=1,2} \alpha_\gamma^{\bar{\mathscr{Q}}} \right) \quad \forall \mathscr{Q} \in \mathbb{P}. \tag{31}$$

The discontinuity sensor in (29) is unreliable when applied to low-order polynomial bases. We therefore recommend that a minimum polynomial order be imposed for this method, say $p_{\min} = 2$. We use the following heuristic for solving a patch of elements to implement the shock-capturing scheme in hyperbolic conduction problems.

(1) Solve the patch with no stabilization.
(2) Use (29) and (30) to compute the sensors and the artificial diffusion for each component of the conservation fields in each element of the patch. Compute the patch-wise maximum diffusion $\alpha^{\mathbb{P}}$ according to (31).
(3) If $\alpha^{\mathbb{P}} = 0$, accept and store the solution from step 1. Otherwise, discard the solution from step 1, assign the diffusivity $\alpha^{\mathbb{P}}$ to all the elements in the patch according to (31), and solve the patch again; store the new solution.
(4) Proceed to the next patch.

4. Adaptive spacetime meshing

An advancing-front procedure for constructing causal spacetime meshes is an essential component of our $\mathscr{O}(N)$ patch-by-patch SDG solution procedure. We summarize in this section methods for unstructured spacetime mesh generation with extensions for adaptive analysis. Although our discussion focuses on meshing domains in 2D $\times$ time, we use the same concepts to address domains in 1D $\times$ time. In principle, the techniques we describe are extensible to domains in 3D $\times$ time, but we have not yet implemented this capability. A more detailed treatment of causal meshing can be found in [46–48,51].

4.1. Causal spacetime meshing

We use an advancing-front mesh generation procedure called Tent Pitcher [52,53] to construct simplicial spacetime meshes that satisfy a patch-wise causality constraint. A 'patch' is a collection of tetrahedral elements. Therefore, the patch boundary is a collection of oriented triangular facets in spacetime. The causality constraint requires that all patch facets are causal, except for those facets that lie on $\partial\mathscr{D}^{\text{nc}}$; any patch that satisfies this requirement is called a causal patch. Inter-element boundaries within a patch are permitted to be non-causal, so the elements within a patch must be solved simultaneously. However, the solution within a patch depends only on data from earlier patches and on prescribed initial and boundary data. This asymmetric dependency implies a partial ordering of patches that enables our $\mathscr{O}(N)$ patch-by-patch solution procedure. Tent Pitcher begins with a triangulation of the spatial domain generated by any available simplicial mesh generator, such as Shewchuk's Triangle [54]. We refer to this mesh as thespace mesh. We append a temporal coordinate to the spatial coordinates of each node in the space mesh; all time coordinates are initialized to the starting time of the analysis interval. Distinct time coordinates become associated with different nodes as the solution evolves, so the space mesh generally describes a spacetime terrain on which time is a nonuniform function of spatial position. The space mesh controls the construction of a spacetime mesh, comprised of $(d+1)$-simplices, as described below.

Tent Pitcher advances a node in the space mesh in time to create a new node in the spacetime mesh. The spacetime segment connecting the node at its previous and new times is called a tent pole. Tent Pitcher constructs a new patch of spacetime elements as the set of tetrahedra that connect the top and bottom of the tent pole to the neighboring nodes in the space mesh. The outflow facets of each new patch must all be causal, and this imposes a local condition on the tent-pole duration that is similar to a CFL condition. However, there is no global time-step restriction as in most explicit time-stepping methods, and the causality constraint derives from the requirements of our patch-by-patch solution procedure, as explained below, and not from a stability condition. Tent

Pitcher repeats this tent-pitching operation to generate a sequence of causal spacetime patches that forms a fully unstructured spacetime mesh. We interleave the mesh generation and solution procedures, computing immediately a patch-wise SDG solution every time Tent Pitcher creates a new patch. This patch-by-patch solution procedure has $\mathcal{O}(N)$ complexity for fixed polynomial order, where N in the number of spacetime patches. A violation of the causality meshing constraint would require a larger cluster of elements to be solved simultaneously, and would thereby destroy the $\mathcal{O}(N)$ complexity property and increase the computational expense. However, stability would not be compromised since the SDG algorithm for each cluster of coupled elements is implicit and unconditionally stable. In fact, the SDG formulation can be used with less complicated meshing procedures, such as simple extrusion of a space mesh in time. Although the solution would be more expensive, the accuracy and element-wise balance properties of the SDG method would be retained.

4.2. Adaptive solution procedure

The goal of our h-adaptive scheme is to divide nearly evenly the finite element error between all of the spacetime elements. We use a residual-based, *a posteriori* error indicator derived from (21). We define a 2-tuple of error indicators for the discrete solution on element $\mathscr{Q}$ as sums of L_1 norms of the volume and boundary residuals.

$$\boldsymbol{\epsilon}^{\mathscr{Q}} = \begin{Bmatrix} \epsilon_1^{\mathscr{Q}} \\ \epsilon_2^{\mathscr{Q}} \end{Bmatrix} := \int_{\mathscr{Q}} |\mathbf{dF} + \mathbf{S}| + \int_{\partial\mathscr{Q}} |\mathbf{F}^* - \mathbf{F}| \tag{32}$$

Based on the definitions of the target fluxes $\mathbf{F}^*$ in (19), the outflow faces do not contribute to the error and can be dropped from the boundary integral in (32). Every time a spacetime patch is solved, we compute the error indicator $\boldsymbol{\epsilon}^{\mathscr{Q}}$ for each element $\mathscr{Q}$ in the patch.

The error indicator (32) drives an extended, adaptive version of the Tent Pitcher meshing algorithm. User-specified parameters $\{\underline{\epsilon}_\gamma, \bar{\epsilon}_\gamma\}_{\gamma=1,2}$ define a target range for the element-wise error, $\underline{\epsilon}_\gamma \leqslant \epsilon_\gamma^{\mathscr{Q}} \leqslant \bar{\epsilon}_\gamma$. Before accepting a new patch solution, we perform checks on each spacetime element $\mathscr{Q}$ in the patch to ensure that the upper inequality is strictly enforced, while taking steps to loosely enforce the lower inequality. If $\epsilon_\gamma^{\mathscr{Q}} > \bar{\epsilon}_\gamma$ for either value of γ, we flag element $\mathscr{Q}$ as needing refinement; if $\epsilon_\gamma^{\mathscr{Q}} < \underline{\epsilon}_\gamma$ for both values of γ, we flag element $\mathscr{Q}$ as coarsenable; otherwise, we flag $\mathscr{Q}$ as needing neither refinement nor coarsening. If any spacetime element in the patch is flagged as needing refinement, we discard the patch solution with all the spacetime elements in the patch and immediately subdivide the corresponding elements in the space mesh using a newest-vertex-bisection algorithm [47]. When the tent-pitching sequence resumes, the causality constraint limits the duration of spacetime elements pitched over the subdivided space elements, resulting in simultaneous refinement in space and time. Coarsening operations are postponed until all the elements surrounding a node in the space mesh are coarsenable. Tent Pitcher then constructs a special spacetime patch that effectively deletes the node from the space mesh, as illustrated in Fig. 3a. The inflow facets of these special patches are fully compatible with the outflow facets of previously-solved patches, so our spacetime coarsening method eliminates the projection errors associated with coarsening operations in most conventional remeshing procedures. Similarly, spacetime implementations of edge-flip and node relocation operations, depicted in Figs. 3b and c, ensure zero projection error in adaptive operations that maintain and improve element quality.

5. Numerical results

In this section, we consider materials with spatially uniform properties and isotropic conductivity tensors given by $\boldsymbol{\kappa} = \kappa\mathbf{I}$, where $\kappa \in \mathbb{R} : \kappa > 0$ and $\mathbf{I}$ is the identity tensor, and present all results in non-dimensional form. We non-dimensionalize temperature and heat flux as

$$\widetilde{T} = \frac{T - T_0}{T_0}, \quad \tilde{\mathbf{q}} = \frac{\mathbf{q}}{T_0 C c}, \tag{33}$$

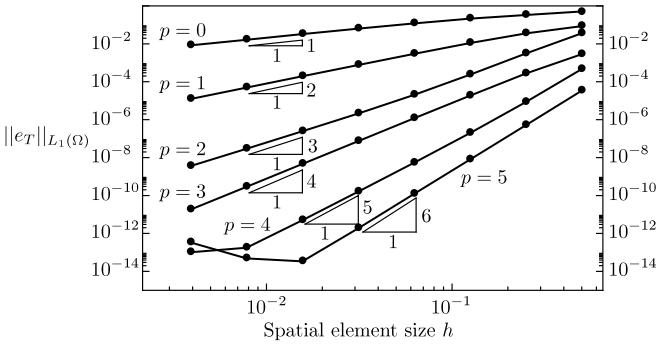

Fig. 4. L_1 norm of terminal thermal error versus element diameter h.

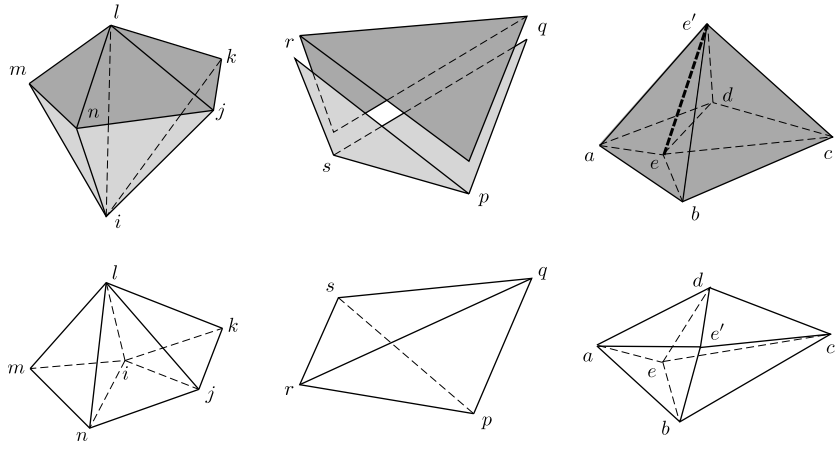

(a) Vertex deletion (degree 5) **(b)** Edge flip **(c)** Inclined tent pole

Fig. 3. Three adaptive meshing operations executed as spacetime patches (above) and as instantaneous operations in space only (below). The coarsening operation (a) deletes a degree-n vertex i to create $n-2$ spacetime tetrahedra: $ijkn$, $ikmn$, and $iklm$. The edge-flip operation (b) uses a single spacetime tetrahedron to switch from edge ps to edge qr, while tent pitching with an inclined tent pole (c) repositions a node from e to e′.

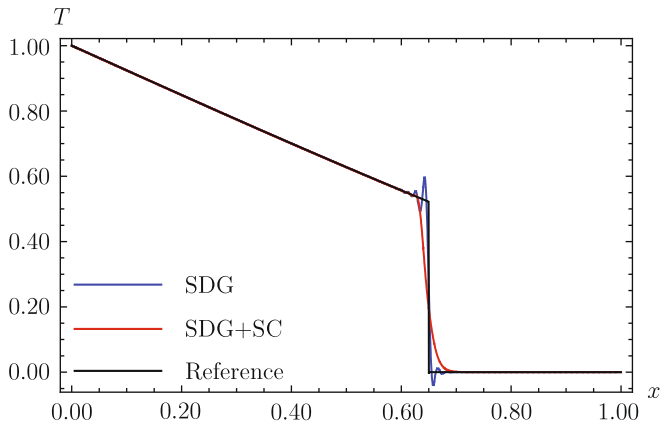

(a) uniform spatial diameter, $h = 0.01$

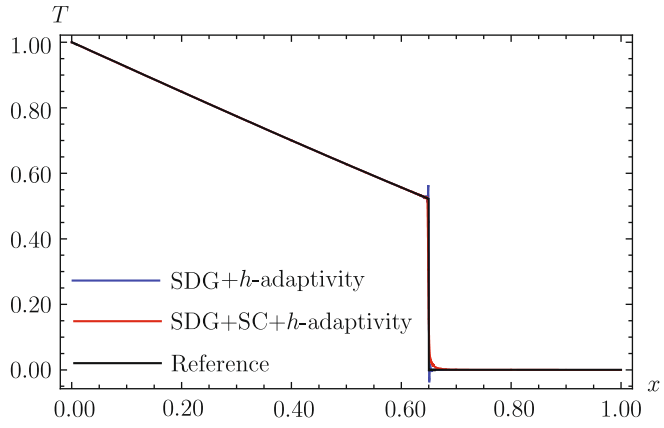

(b) h-adaptive SDG solution

Fig. 5. Effects of shock-capturing operator (SC) and h-adaptive meshing on SDG solution at $t = 0.65t_L$. Reference solution is T_{RS} computed with $n = 5 \times 10^4$.

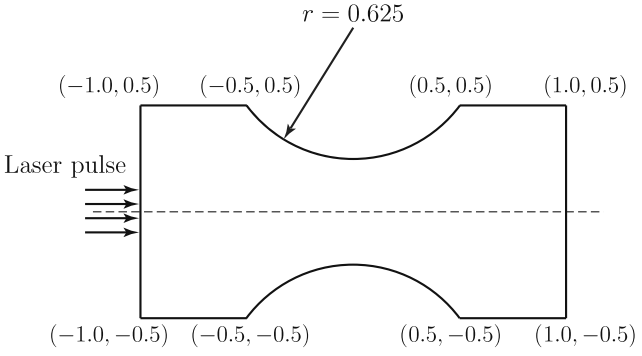

(a) Converging–diverging channel; pulsed-laser heating

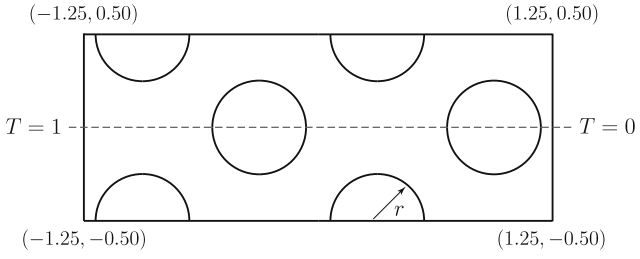

(b) Material with circular voids or inclusions

Fig. 6. Analysis domains and loading for 2D examples.

where T_0 is a non-zero reference temperature, and scale the space-time coordinates according to

$$\tilde{x}_i = \frac{x_i}{\tau c}, \quad \tilde{t} = \frac{t}{\tau}. \tag{34}$$

Many authors, dating back to [55], introduce a factor of 2 in the temporal and spatial non-dimensionalization, yielding

$$\tilde{t} = \frac{t}{2\tau}, \quad \tilde{x}_i = \frac{x_i}{2\tau c}. \tag{35}$$

Although the "natural" coordinate non-dimensionalization is that of (34), we find it convenient, for purposes of comparison with results in the literature, to sometimes work with the non-dimensional coordinates of (35). Our convergence study in Section 5.1 is non-dimensionalized according to (33) and (34); the remainder of our results are given using (33) and (35). For convenience, we drop the tildes from the non-dimensional quantities from here on.

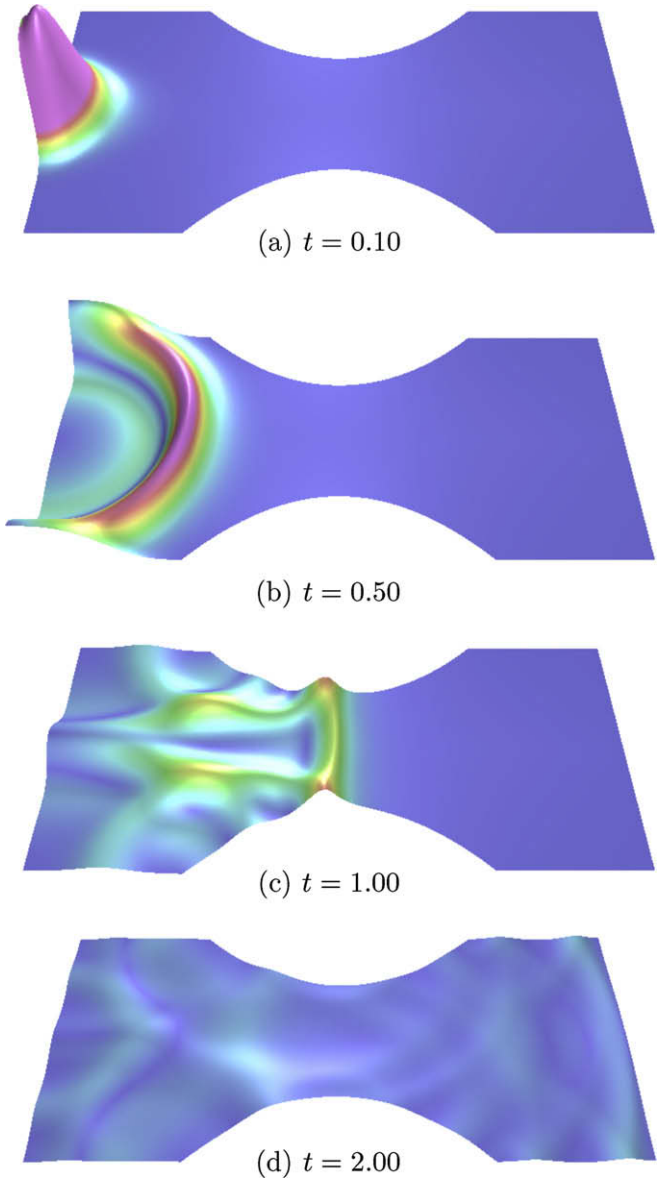

Fig. 7. Temperature evolution (color and height) for channel domain heated by Gaussian laser pulse.

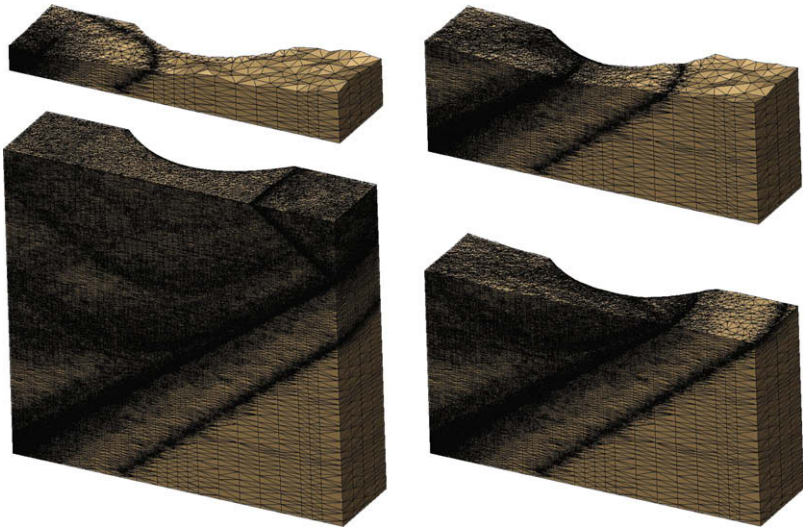

Fig. 8. Evolution of adaptive spacetime mesh for converging-diverging channel problem. Clockwise from top-left: mesh status after solution of 1 million, 5 million, 10 million and 16,489,813 elements.

5.1. Convergence study in one spatial dimension

Palaniappan et al. [51] demonstrated that the SDG method applied to scalar conservation laws delivers the optimal convergence rate of $O(h^{p+1})$ in the L_1 error norm, where h is the maximum element diameter, in regions where the solution is smooth. The present formulation involves a system of conservation laws with solution-dependent source terms, a class of problems that is somewhat different from those considered in [51]. In this section, we demonstrate that the convergence rate of the SDG method for the MCV problem is also $O(h^{p+1})$ for smooth solutions. To facilitate our convergence study, we examine a problem in one spatial dimension ($d = 1$) for which an analytical solution is available. The problem domain is $\mathscr{D} := \{(x,t) : x \in [0,1], t \in [0,1]\}$. The boundary and initial conditions are specified as $T(0,t) = 0$, $T(1,t) = 0$, $q(x,0) = 0$ and $T(x,0) = \sin(\pi x)$. The exact solution satisfying (17) and the prescribed data is

$$T(x,t) = \left[\cos(\omega t) + \frac{1}{2\omega}\sin(\omega t)\right]\sin(\pi x)\mathrm{e}^{-t/2}, \tag{36a}$$

$$q(x,t) = -\frac{\pi}{\omega}\cos(\pi x)\sin(\omega t)\mathrm{e}^{-t/2}, \tag{36b}$$

where $\omega = (\sqrt{4\pi^2 - 1})/2$.

We define the thermal error, $e_T := T_{\mathrm{R}} - T$ in which a subscript 'R' identifies components of the reference solution (36) and T is the SDG finite element approximation, and compute the L_1-norm of the terminal thermal error on $\Omega := \{(x,1) \in \partial\mathscr{D}\}$. In all cases, we use structured spacetime meshes in which all of the triangular elements are geometrically similar. Fig. 4 indicates that the optimal convergence rates of $O(h^{p+1})$ are achieved and that errors on the order of machine precision are obtained on meshes with sufficient refinement for $p = 4, 5$. Similar results (not shown) demonstrate that the MCV error, $e_q := q_{\mathrm{R}} - q$, attains the same optimal convergence rates.

5.2. Shock capturing in 1D

Although the SDG shock capturing operator introduced in 3.3 is not required for numerical stability, it can be used to eliminate undesirable over- and under-shoot in the vicinity of solution discontinuities. Here we demonstrate the effects of the shock-capturing operator in a simple, one-dimensional example; see [44] for more detailed studies of the shock-capturing operator as applied to systems of nonlinear conservation laws.

The problem domain for this example is $\mathscr{D} := \{(x,t) : x \in [0,L], t \in [0,t_f]\}$. The boundary conditions are $T(0,t) = 1$ and $T(L,t) = 0$, while zero initial data are prescribed for both T and q. The incompatible initial and boundary data at $(x,t) = (0,0)$ generates a traveling discontinuity in the solution that arrives at $x = L$ at time $t_L = L/c$, in which c is the thermal wave speed, *cf.* 1.1. For $t < t_L$, the solution to the present problem coincides with the solution to a problem posed on the quarter-spacetime, $\mathscr{D}' := \{(x,t) : x, t > 0\}$ with the same properties and boundary conditions, except $L = \infty$. Thus, we use the solution to the quarter-spacetime problem as a reference solution for times $t < t_L$.

Tzou [56] treats the half-space problem in a semi-analytic fashion. After non-dimensionalizing according to (33) and (35), he invokes a temporal Laplace transform. The solution to the transformed equation is straightforward, but the inverse Laplace transform is not. To overcome this difficulty, Tzou introduces a Riemann sum approximation for the inversion. For the present set of boundary conditions, the transformed solution and its approximated inverse are

$$\overline{T}(x,k) = \frac{1}{k}\mathrm{e}^{-x\sqrt{k(k+2)}}, \tag{37}$$

$$T_{\mathrm{RS}}(x,t) = \frac{\mathrm{e}^{\gamma t}}{t}\left[\frac{1}{2}\overline{T}(x,\gamma) + \mathrm{Re}\left\{\sum_{n=1}^{N}(-1)^n\overline{T}(x,\gamma + in\pi/t)\right\}\right], \tag{38}$$

where 'Re' denotes the real part, k is the Laplace transform of t and $\gamma = 4.7/t$. The subscript RS denotes the Riemann-sum approximation to the exact solution.

Fig. 5 displays plots of the SDG solution, with and without shock capturing, and the reference Riemann-sum approximation T_{RS} at $t = 0.65t_L$. The values of the shock-capturing parameters are $C_\alpha = 1$, $C_s = 1/4$ and $\beta = 2$. Fig. 5a demonstrates the ability of the shock-capturing operator to suppress overshoot and undershoot at the discontinuity without polluting the rest of the solution. In these simulations, we use a non-adaptive mesh with uniform spatial diameter $h = 0.01$, leading to a total of 9,900 quartic (*i.e.*, $p = 4$) spacetime elements. The terminal error norm is $\|e_T\|_{L_1(\Omega)} = 5.339 \times 10^{-3}$.[4]

[4] The L_1 error computations were computed using Mathematica. Due to the highly oscillatory nature of the Riemann-sum solution, these integrals are not exact, but are correct to within the significant digits reported here.

Fig. 5b shows the ability of an *h*-adaptive SDG solution with shock capturing to more accurately capture the discontinuity while suppressing the overshoot and undershoot that persist when *h*-adaptive methods are applied alone. The adaptive error tolerances, $\underline{\epsilon} = 0.60 \times 10^{-5}$ and $\bar{\epsilon} = 1.4 \times 10^{-5}$, generate an unstructured spacetime mesh containing 16,035 elements (a total of

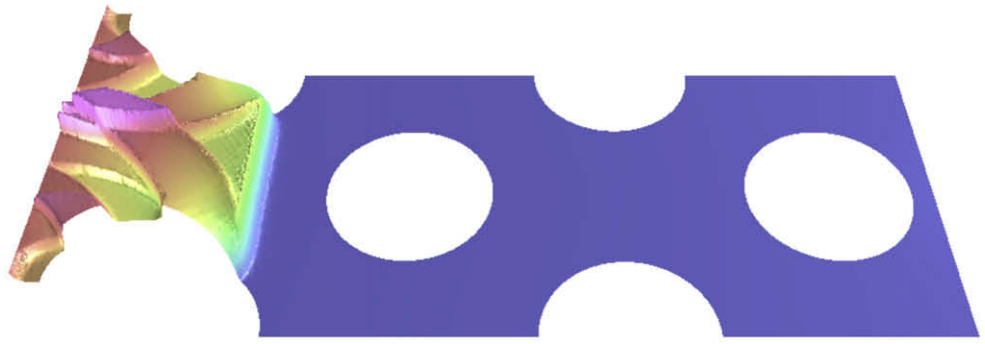

(a) $t = 0.50$

(b) $t = 0.75$

(c) $t = 1.00$

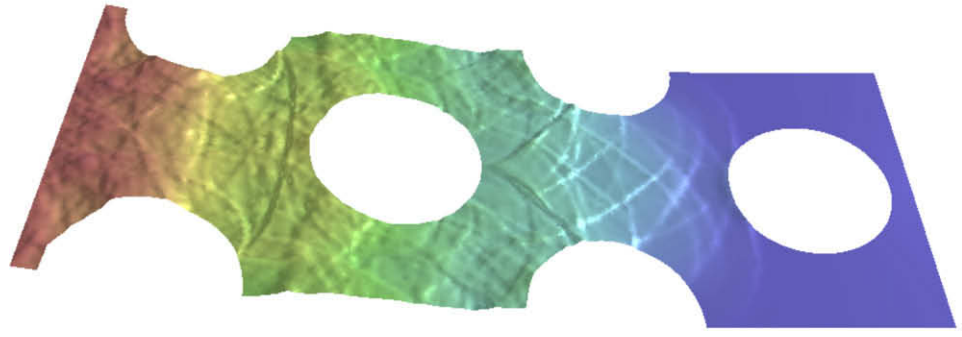

(d) $t = 2.00$

Fig. 9. Temperature evolution (color and height) for a domain with circular voids.

18,790 elements were solved including those discarded for refinement), yielding a terminal error norm for the adaptive case of $\|e_T\|_{L_1(\Omega)} = 8.739 \times 10^{-4}$.[4] Thus, the adaptive simulation decreases the error by over a factor of 6 while increasing the analysis cost by less than a factor of 2.

5.3. Two-dimensional study of Gaussian laser-pulse heating

The first of the two-dimensional examples we present is a converging–diverging channel problem identical to the one solved in [34]. The analysis domain, shown in Fig. 6a, is symmetric about the x-axis; we exploit this symmetry in our computations and model only the top half (*i.e.*, $y > 0$) of the domain. The laser pulse incident on the left side of the domain is modeled as a non-dimensional Gaussian-type body heat source,

$$Q(x,y,t) = \frac{1}{2\Delta t_{\mathrm{p}}} \exp\left[-\frac{1+x}{\Delta} - \frac{y^2}{\Delta_r^2} - \left(\frac{t}{t_{\mathrm{p}}}\right)^2\right], \tag{39}$$

where Δ is the penetration depth, Δ_r is the width of the laser beam and t_{p} is the characteristic duration of the laser pulse. In this study, we specify $\Delta = 0.05$, $\Delta_r = 0.10$ and $t_{\mathrm{p}} = 0.10$. The material parameters are the same as in the previous example, and we impose homogeneous initial conditions. We use cubic (*i.e.*, $p = 3$) spacetime elements and enable h-adaptive meshing with $\underline{\epsilon} = 0.60 \times 10^{-8}$ and $\bar{\epsilon} = 1.4 \times 10^{-8}$. This problem has a smooth solution, so the SDG shock-capturing operator is inactive.

Fig. 7 shows a time sequence of the evolving temperature distribution within the channel domain. These images of the solution fields, as well as those in subsequent examples, are generated with the per-pixel accurate rendering system described in [57]. The numerical results from our SDG simulation are reflected about the x-axis in the visualizations to show the complete problem domain. At $t = 0.10$, the thermal response reflects the Gaussian distribution of the laser-pulse irradiation. The second plot, at time $t = 0.50$, shows thermal waves propagating away from the source, with lower temperatures in the region of the heat source. The plot at $t = 1.00$ depicts the heat wave traversing the middle of the channel; reflections from the boundaries are clearly visible. The heat pulse reaches the right edge of the domain at $t = 2.00$ in the final plot. The temperature distribution is not yet uniform throughout the body, but the temperature range is significantly reduced compared to early times. Our results are broadly similar to those reported in [34], although the SDG solution generally predicts sharper wavefronts and resolves a number of fine-scale solution features that are absent in [34]. We attribute these differences to our use of higher-order spacetime elements in a relatively well-resolved, adaptively-refined mesh. Although there is insufficient information available for a quantitative comparison of efficiency, we note that our adaptive solution procedure generates 16,489,813 cubic spacetime elements, while [34] used over 7000 linear triangular elements in a non-adaptive space mesh and an unspecified number of forward-Euler time steps. This example shows that our results are at least in general agreement with published results for the hyperbolic thermal model. It also demonstrates the influence of interacting waves on the temperature distribution, an effect that Fourier's law cannot capture.

Fig. 8 illustrates our h-adaptive, advancing-front analysis procedure. Dense mesh regions, filled with small-diameter, short duration elements, cover the trajectories of sharp solution features to accurately resolve moving wavefronts. However, these elements do not impose a global restriction on element durations; larger elements with much longer durations reduce the cost of analysis in regions where the solution is less sharply graded. The clear correlation between significant solution features and the mesh-density pattern demonstrates the effectiveness of our adaptive error indicator.

5.4. Effect of voids and inclusions on heat conduction

This set of examples demonstrates the ability of the SDG method to model more complex domains and boundary conditions as well as its ability to capture sharp solution fronts with shock capturing and h-adaptive meshing. We consider a material containing circular voids or inclusions, as depicted in Fig. 6b. Matrix material surrounds circular features with radius $r = 1/2$. We apply homogeneous initial conditions and impose Dirichlet temperature boundary conditions, $T = 1$ and $T = 0$ along the top and bottom edges, respectively. The domain is symmetric about the y axis, so we only model the half where $x > 0$ with symmetry conditions along the $x = 0$ and $x = 1/2$ boundaries.

5.4.1. Material with circular voids

In this example, we use homogeneous Neumann (zero heat flux) conditions along the circular boundaries to model the effects of voids. We use cubic (*i.e.*, $p = 3$) spacetime elements and activate the h-adaptive analysis scheme with $\underline{\epsilon} = 4.50 \times 10^{-8}$ and $\bar{\epsilon} = 1.05 \times 10^{-7}$. The resulting spacetime mesh contains 14,832,534 tetrahedral elements. The shock-capturing parameters are $C_\alpha = 1$, $C_s = 1$ and $\beta = 2$.

Fig. 9 shows a time sequence of the temperature distribution in which temperature is mapped to both the height and color fields in the visualizations. A right-propagating thermal shock, due to the non-zero Dirichlet loading along the left edge, is visible at time $t = 0.50$ with little evidence of diffraction by the voids. However, edge effects and reflections off the void boundaries are clearly evident behind the shock front. Temperatures higher than the prescribed boundary values are present due to wave interactions.

Fig. 10. Comparison of a material with voids (left) to a homogeneous strip (right) at $t = 3.75$. The homogeneous strip shows a wavefront still present. Reflections and diffraction due to the voids, in combination with intrinsic diffusion, eliminate the wavefront in the perforated material.

The visualization at $t = 0.75$ shows early reflections of the leading thermal wavefront off the boundary of the left-center void; diffraction effects are clearly evident. Waves behind the front continue to interact and reflect off the void boundaries, creating an increasingly complex thermal distribution. As the thermal profile evolves to $t = 1.00$, the waves behind the front continue to interact, although the magnitudes of individual waves decrease. Sharp wavefronts traveling at the sides of the center void are still visible. The leading thermal waves reach the right-center void in the final visualization, at time $t = 2.00$. The temperature gradients behind the front continue to decrease, due to both intrinsic diffusion and the increasing number of wave interactions.

This example demonstrates the effects of non-uniform geometry on the dissipation of a temperature discontinuity. We illustrate this point in Fig. 10, where we compare at time $t = 3.75$ the response of the material with voids to that of a strip of homogeneous

(a) $t = 0.625$

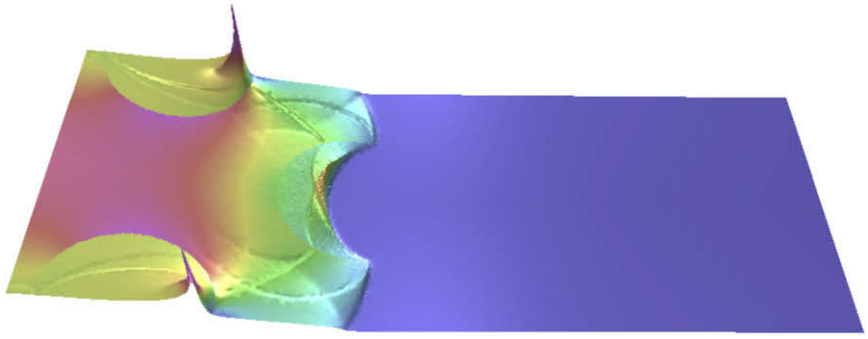

(b) $t = 1.000$

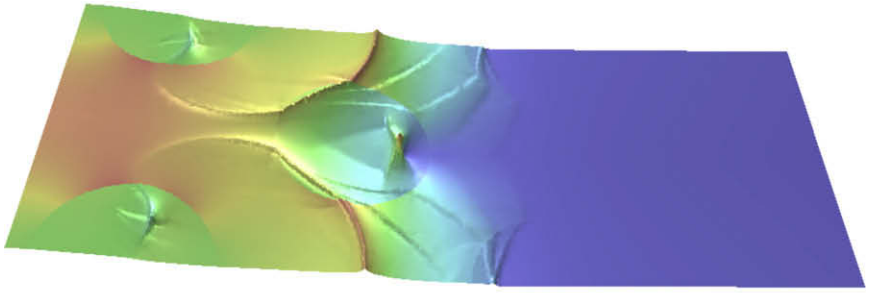

(c) $t = 1.500$

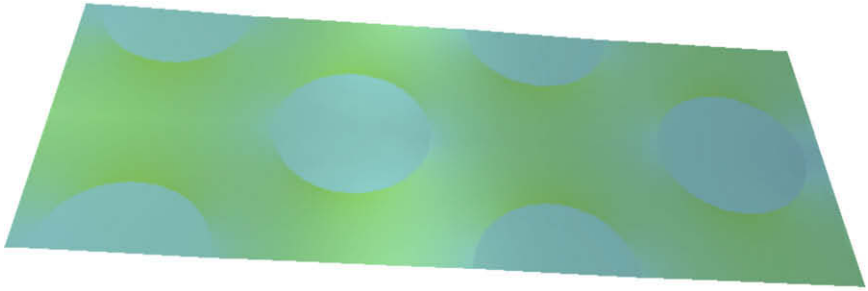

(d) $t = 6.000$

Fig. 11. Time sequence of T (height) and $|\mathbf{q}|$ (color) for composite material system.

material subjected to identical loading. A thermal shock front is still visible in the solution for the homogeneous strip, whereas no such discontinuity is evident in the solution for the material with voids. Both solutions reflect the diffusion that is implicit in the governing equations. However, the absence in the perforated material of an unobstructed trajectory for the initial thermal wavefront leads to complex wave interactions that cause the temperature profile to approach a uniform gradient more rapidly than in the homogeneous medium.

5.4.2. Composite material with circular inclusions

In this final example, we examine the effects of hyperbolic heat conduction on a bimaterial system comprised of circular inclusions embedded in a matrix. We use subscripts 1 and 2 to denote, respectively, quantities associated with the matrix and inclusion materials. The non-dimensionalization, given by (33) and (35), is with respect to the properties of the matrix material. The matrix and inclusion parameters are related by $\kappa_2/\kappa_1 = 1/2$, $\tau_2/\tau_1 = 1$ and $C_2/C_1 = 2$. The resulting thermal wave speeds are $c_1 = 1$ and $c_2 = 1/2$. We use Riemann fluxes for bimaterial interfaces, *cf.* Appendix B.2, on the boundaries between the matrix and the inclusions. The element polynomial order, the adaptive error tolerances and the shock-capturing parameters are the same as in the previous example. The resulting spacetime mesh, which now covers both the matrix and the inclusions, contains a total of 17,145,419 tetrahedral elements.

Fig. 11 displays a sequence of visualizations of the temperature field and the heat-flux magnitude, with T mapped to height and $|\mathbf{q}|$ to color. The first three images display the wave-like evolution at early times, while the fourth image displays the diffuse solution after steady-state conditions are attained. In all the images, we observe that the $\boldsymbol{F}_\eta$ component of the jump condition (17b) enforces continuity of temperature when applied to the vertical (in spacetime) bimaterial interfaces. Although the jump condition on $\boldsymbol{F}_e$ similarly enforces continuity of the normal component of $\mathbf{q}$ across the bimaterial interfaces, this does not imply continuity of $|\mathbf{q}|$. Accordingly, the color fields in the images exhibit discontinuities.

At time $t = 0.625$, the initial wavefront is transiting the top row of inclusions. The effects of the distinct wave speeds in the bimaterial system are clearly evident; refraction generates curved, lagging wavefronts within the inclusions as the faster waves in the matrix diffract around the inclusion boundaries. Reflections off the inclusion boundaries and waves due to edge effects along the top Dirichlet boundary are also visible within the matrix. At $t = 1.00$, the leading wavefront impinges on the second row of inclusions.

By the Maximum Principle, we know that no local extrema are possible on the interior of the spacetime domain $\mathscr{D}$ via the parabolic Fourier conduction model in the absence of heat sources Q. This is not the case for the hyperbolic MCV model, as is dramatically demonstrated in Fig. 11b. Here, the curved wavefronts within the top row of inclusions converge to a point, causing sharp spikes in both the temperature and flux fields. This focusing effect generates a peak temperature of $T = 2.096$ at $t = 0.994$, more than double the maximum Dirichlet boundary value, $T = 1.0$. Part of the energy amassed in the spikes is transmitted to the matrix in the form of sharp radial wavefronts that impinge on the central inclusion in Fig. 11c, within which a new spike is forming.

In the final plot at $t = 6.0$, the solution has reached a steady state, and the temperature field shows no visible perturbations from a uniform gradient. The composite material channels most of the thermal flow through the more conductive matrix. Although flux concentrations are evident where the more resistive inclusions constrict the flow, the peak values of $|\mathbf{q}|$ are substantially smaller than in the early stages of the simulation. At this stage, we have $\dot{\mathbf{q}} \approx \mathbf{0}$, so the MCV equation (2) agrees with the Fourier conduction model, and the long-term hyperbolic and parabolic solutions match.

Comparing the results of this simulation to those presented in Fig. 9, we observe that the inclusions have a diffusive effect that suppresses the complex wave patterns generated by reflection and diffraction in the material with voids. In general, sharp wavefronts tend to dissipate more rapidly in the composite system, so less mesh refinement is required to resolve the solution as the simulation advances. Thus, even though the spacetime mesh in this example covers a larger domain than the one used in the example described in Section 5.4.1, there is only a modest increase in the number of tetrahedral elements.

6. Conclusions

We have presented a new spacetime discontinuous Galerkin method for hyperbolic heat conduction using the MCV equation. The SDG formulation guarantees element-wise conservation with respect to Riemann fluxes and prescribed data on the element boundaries. A causal spacetime meshing procedure and a patch-by-patch solution scheme yield a method with $\mathscr{O}(N)$ complexity that can handle models with tens of millions of spacetime elements on single-processor systems. Since multiple patches can be pitched and solved simultaneously, the SDG method is well-suited to asynchronous, parallel implementations that could support even larger problem sizes. Work on a fully-adaptive, parallel implementation is in progress and will be reported in a later paper.

The SDG formulation supports element basis functions of arbitrarily high polynomial order without expanding the stencil. This is in contrast to, for example, finite volume methods where expanding stencils limit the efficiency of higher-order models. Our numerical experiments confirm optimal convergence rates of $\mathrm{O}(h^{p+1})$ in L_1 error norms for problems with smooth solutions. Although the SDG method does not require stabilization for the MCV equation, the SDG shock-capturing operator can be used to eliminate overshoot and undershoot in the vicinity of solution discontinuities. A robust shock indicator for the case of first-order polynomials would improve the efficiency and flexibility of our method; this is the subject of on-going research.

An improved Tent Pitcher algorithm with h-adaptive extensions accurately captures sharp solution features while maintaining reasonable solution cost. Spacetime implementations of common adaptive meshing operations, including vertex deletion, edge flips and vertex smoothing, circumvent the projection errors that are unavoidable when these operations are implemented in space only. This approach preserves the optimal convergence rates of high-order SDG models, while the projection errors in conventional remeshing techniques can be no better than $\mathscr{O}(h)$. Adaptive error checks and remeshing are implemented locally at the patch level in a patch-by-patch solution procedure, so that remeshing proceeds continuously throughout the solution process. This fine-grained approach to remeshing yields an efficient adaptive algorithm, as only a small amount of computational effort is discarded when a patch solution is rejected for exceeding the error tolerances.

Our current h-adaptive algorithm is reasonably efficient for problems with smooth solutions where regularity does not limit the convergence rate for higher-order elements. However, the MCV model admits solutions with discontinuities, where regularity limits the convergence rate to $\mathrm{O}(h/p)$ in the SDG shock-capturing method. Thus, higher-order elements are inefficient in the vicinity of discontinuous features, as their cost grows more rapidly than the error reduces for larger values of p. Therefore, an hp-adaptive implementation of the SDG method, in which high-order elements are used in smooth regions and low-order elements are used near discontinuities, should yield significant efficiency gains over our current implementation.

The two-dimensional numerical examples in this work illustrate the distinct physics captured by the MCV equation and Fourier's law. Studies of materials with voids and inclusions demonstrate the ability of the SDG method to handle non-trivial domain geometries and to incorporate bimaterial interfaces in a straightforward manner. The finite wave speeds implicit in the MCV equation create a complex pattern of wave interactions and boundary reflections that are absent in models based on the classical heat equation. This wave-like behavior leads to thermal response that is qualitatively different from that generated by parabolic conduction models. For example, the MCV model predicts temperatures well above the maximum boundary data in problems with Dirichlet loading as well as uneven heating of matrix material and inclusions in bimaterial systems.

The adaptive SDG model for hyperbolic heat conduction delivers high-precision solutions for applications defined at very small length and time scales where wave-like thermal response is important and the Fourier conduction model's adherence to the Maximum Principle renders it a non-conservative approximation. A thermomechanical model using the MCV conduction equation is an important extension that will be reported in a forthcoming paper; extensions to accommodate nonlinear thermal response would also be of interest. Potential applications of this technology include simulations of pulsed-laser heating of thin films, MEMS and electronics fabrication processes, integrated circuit chips and cryogenic cooling [34]. Concurrent coupling of atomistic and continuum models is another promising application; the thermal component of a hyperbolic thermomechanical model could account for the energy associated with high-frequency atomistic motions that cannot be resolved in the continuum.

Acknowledgements

The authors gratefully acknowledge the contributions of Shuo-Heng Chung, Jayandran Palaniappan, and Yuan Zhou. Support was provided by the Center for Process Simulation and Design (CPSD) and the Materials Computation Center (MCC) at the University of Illinois at Urbana-Champaign under NSF Grant numbers ITR/AP DMR 01-21695 and ITR/AP DMR 03-25939.

Appendix A. Discrete weak form in indicial notation

In this appendix, we present the discrete weak form (26) in indicial notation. Commas as subscripts denote partial derivatives with respect to the variable appearing after the comma, and a superposed dot indicates partial differentiation with respect to the temporal variable. The definitions of the fluxes and source terms from (14) and (15) are substituted in for clarity. The discrete weak form in indicial notation is

$$\begin{aligned}\int_{\mathcal{Q}} \{ & -\dot{\omega} C T + \omega_j [\alpha^{\mathcal{Q}} \delta^{jk} (CT)_{,k} - q^j] + \omega Q - \dot{w}^j \lambda_{jk} \tau q^k \\ & - w^j_{,j} T + \alpha^{\mathcal{Q}} w^j_{,m} \delta^{mn} (\lambda_{jk} \tau q^k)_{,n} + w^j \lambda_{jk} q^k \} \, \mathrm{d}V \\ & + \int_{\partial \mathcal{Q}} \{ [(\omega (q^{*j} - \alpha^{\mathcal{Q}} p_1^{*j}) + w^j T^*) \delta_{jk} - w^j \alpha^{\mathcal{Q}} (p_2^*)_{jk}] n^k \\ & + [\omega C T^* + w^j \lambda_{jk} \tau q^{*k}] n^t \} \, \mathrm{d}S = 0 \quad \forall (\omega, \mathbf{w}) \in \mathcal{V}_h^{\mathcal{Q}} \end{aligned} \tag{A.1}$$

in which n^t and n^m are the temporal and spatial components of the unit spacetime normal vector $\mathbf{n}$ defined as outward on $\partial\mathcal{Q}$, and λ_{jk} and $(p_2^*)_{jk}$ are covariant components of the tensors $\boldsymbol{\lambda}$ and $\mathbf{p}_2^*$.

In this rendering of the SDG formulation, we artificially treat spacetime as a manifold in an Euclidean space of dimension $d+1$ to uniquely determine the spacetime unit normal vector $\mathbf{n}$. This requires that we select a positive reference velocity to resolve the dimensional differences between space and time coordinates. Although the choice of the reference velocity is entirely arbitrary, the validity of the resulting formulation is independent of its value. Our use of exterior calculus on manifolds in the main formulation circumvents these complications, allowing us to work directly in the natural vector space for this problem, $\mathbb{E}^d \times \mathbb{R}$.

Appendix B. Riemann fluxes

The definitions of the Riemann fluxes (denoted with superscript R) complete the formulation. In view of the linearity of the problem, we have

$$\mathbf{F}^R(T, \mathbf{q}) = \mathbf{F}(T^R, \mathbf{q}^R) \tag{B.1}$$

for both the homogeneous and bimaterial interfaces considered in this paper. Thus, this appendix presents expressions for the Riemann values of the temperature T^{R} and the heat flux vector $\mathbf{q}^{\mathrm{R}}$ for spatial dimension $d = 1, 2$. We also present Riemann values for vertical bimaterial interfaces, *cf.* Section 5.4.

We introduce notation for jump and average operators, $[\![f]\!] = f_\beta - f_\alpha$ and $\langle\!\langle f \rangle\!\rangle = \frac{1}{2}(f_\beta + f_\alpha)$, where subscripts α and β refer to traces from opposite sides of a spacetime interface.

B.1. Riemann values on 1-manifolds in $\mathbb{E}^1 \times \mathbb{R}$

Consider a causal patch of elements on $\mathbb{E}^1 \times \mathbb{R}$, as depicted in Fig. B.1. The Riemann values on $\Gamma_{\alpha\beta}$ are functions of the traces of the temperature and heat flux vector fields from the adjacent elements, $\mathcal{Q}_\alpha$ and $\mathcal{Q}_\beta$. We obtain the Riemann values as the solution to a local Riemann problem defined on the configuration shown at the right in Fig. B.1. For a homogeneous interface with $|m| \leqslant |c|$, the Riemann values are

$$T^R(x,t) = \langle\!\langle T \rangle\!\rangle - \frac{z}{2}[\![q]\!] \quad q^R(x,t) = \langle\!\langle q \rangle\!\rangle - \frac{1}{2z}[\![T]\!], \tag{B.2}$$

where $z = \sqrt{\tau/\kappa C}$ and the wavespeed $c = \sqrt{\kappa/\tau C}$. The Riemann values change slightly for a bimaterial interface with $m = 0$. To compute these values, we follow the procedure outlined in [27] to obtain

$$T^R(x,t) = \frac{1}{z_\alpha + z_\beta}(z_\alpha T_\beta + z_\beta T_\alpha - z_\alpha z_\beta [\![q]\!]), \tag{B.3a}$$

$$q^R(x,t) = \frac{1}{z_\alpha + z_\beta}(z_\alpha q_\alpha + z_\beta q_\beta - [\![T]\!]), \tag{B.3b}$$

where the subscripts α and β indicate the side (material) from which the trace is taken.

B.2. Riemann values on 2-manifolds in $\mathbb{E}^2 \times \mathbb{R}$

Consider a causal patch of elements in $\mathbb{E}^2 \times \mathbb{R}$, as depicted in Fig. B.2a. The noncausal interface $\Gamma_{\alpha\beta}$ is the common boundary between two elements in the patch, $\mathcal{Q}_\alpha$ and $\mathcal{Q}_\beta$. We introduce a new pair of spatial coordinates (ξ_1, ξ_2) to facilitate the formulation of a one-dimensional Riemann problem on $\Gamma_{\alpha\beta}$. The second coordinate, ξ_2, is the spatial vector that is tangent to $\Gamma_{\alpha\beta}$; ξ_1 is the spatial

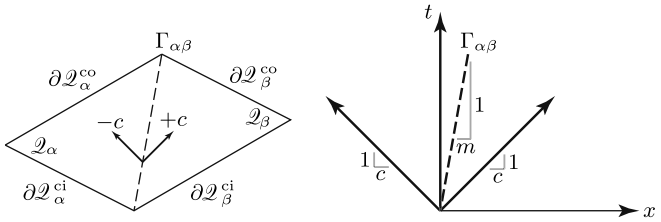

Fig. B.1. Causal patch of elements in $\mathbb{E}^1 \times \mathbb{R}$ with non-causal interface $\Gamma_{\alpha\beta}$.

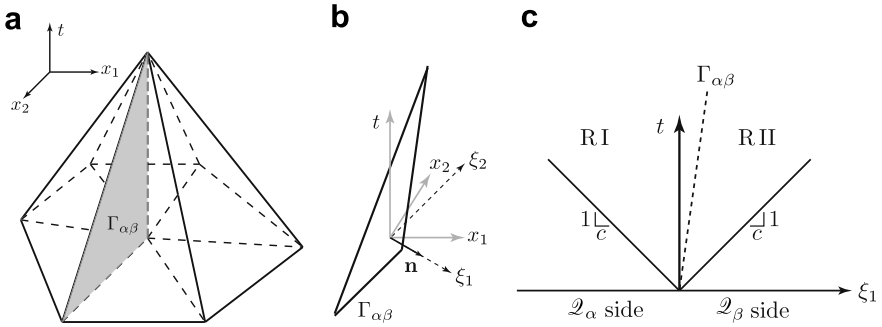

Fig. B.2. Causal patch of elements in $\mathbb{E}^2 \times \mathbb{R}$: (a) non-causal interface $\Gamma_{\alpha\beta}$; (b) global and local coordinates on $\Gamma_{\alpha\beta}$; (c) Riemann problem in the ξ_1 direction.

vector that is orthogonal to ξ_2 and that points outward from $\mathscr{Q}_\alpha$. Let the spatial normal vector $\mathbf{n}$ be the vector with unit magnitude in the direction of ξ_1. Fig. B.2b illustrates the (ξ_1, ξ_2)-coordinate system and the spatial normal vector $\mathbf{n}$.

We solve a one-dimensional Riemann problem in the direction of $\mathbf{n}$ (*cf.* Abedi et al. [46]). There are two branches to the solution, depending on the inclination of $\Gamma_{\alpha\beta}$ and which of two regions, RI and RII shown in Fig. B.2c, it lies in. If $\Gamma_{\alpha\beta}$ is vertical and lies on the boundary between the two regions, the solution from either branch may be used as they generate identical Riemann fluxes for this orientation. We introduce the following quantities to obtain a concise notation: $\mu = \boldsymbol{\kappa}(\mathbf{n}) \cdot \mathbf{n}$, $z = \sqrt{\tau\mu/C}$, and the wavespeed $c = \sqrt{\mu/\tau C}$. The Riemann values for a homogeneous interface are:

$$T^R = \langle\!\langle T \rangle\!\rangle - \frac{z}{2\mu}[\![\mathbf{q}]\!] \cdot \mathbf{n} \quad \text{if } \Gamma_{\alpha\beta} \text{ is in RI or RII,} \tag{B.4a}$$

$$\mathbf{q}^R = \begin{cases} \mathbf{q}_\alpha - \frac{1}{2}(z^{-1}[\![T]\!] - \mu^{-1}[\![\mathbf{q}]\!] \cdot \mathbf{n})\boldsymbol{\kappa}(\mathbf{n}) & \text{if } \Gamma_{\alpha\beta} \text{ is in RI,} \\ \mathbf{q}_\beta - \frac{1}{2}(z^{-1}[\![T]\!] + \mu^{-1}[\![\mathbf{q}]\!] \cdot \mathbf{n})\boldsymbol{\kappa}(\mathbf{n}) & \text{if } \Gamma_{\alpha\beta} \text{ is in RII.} \end{cases} \tag{B.4b}$$

The numerical results presented in 5.4.2 require the Riemann values for a vertical bimaterial interface. Again, we follow the procedure in [27] to obtain

$$T^R = \frac{1}{z_\alpha\mu_\beta + z_\beta\mu_\alpha}\left(z_\alpha\mu_\beta T_\beta + z_\beta\mu_\alpha T_\alpha - z_\alpha z_\beta[\![\mathbf{q}]\!] \cdot \mathbf{n}\right) \quad \text{if } \Gamma_{\alpha\beta} \text{ is in RI or RII,} \tag{B.5a}$$

$$\mathbf{q}^R = \begin{cases} \mathbf{q}_\alpha - \frac{1}{z_\alpha\mu_\beta + z_\beta\mu_\alpha}(\mu_\beta[\![T]\!] - z_\beta[\![\mathbf{q}]\!] \cdot \mathbf{n})\boldsymbol{\kappa}(\mathbf{n}) & \text{if } \Gamma_{\alpha\beta} \text{ is in RI,} \\ \mathbf{q}_\beta - \frac{1}{z_\alpha\mu_\beta + z_\beta\mu_\alpha}(\mu_\alpha[\![T]\!] + z_\alpha[\![\mathbf{q}]\!] \cdot \mathbf{n})\boldsymbol{\kappa}(\mathbf{n}) & \text{if } \Gamma_{\alpha\beta} \text{ is in RII.} \end{cases} \tag{B.5b}$$

It is straightforward to show that (B.4) reduces to (B.5) when the materials on opposing sides of an interface are identical.

References

[1] V.A. Bubnov, Wave concepts in the theory of heat, Int. J. Heat Mass Transf. 19 (1976) 175–184.
[2] D.D. Joseph, L. Preziosi, Heat waves, Rev. Mod. Phys. 61 (1) (1989) 41–73.
[3] D.D. Joseph, L. Preziosi, Addendum to the paper "Heat waves", Rev. Mod. Phys. 62 (2) (1990) 375–391.
[4] C.C. Ackerman, B. Berman, H.A. Fairbank, R.A. Guyer, Second sound in solid helium, Phys. Rev. Lett. 16 (18) (1966) 789–791.
[5] H.E. Jackson, C.T. Walker, T.F. McNelly, Second sound in NaF, Phys. Rev. Lett. 25 (1) (1970) 26–28.
[6] V. Narayanamurti, R.C. Dynes, Observation of second sound in bismuth, Phys. Rev. Lett. 28 (22) (1972) 1461–1465.
[7] J.C. Maxwell, On the dynamical theory of gases, Philos. Trans. Roy. Soc. Lond. 157 (1867) 49–88.
[8] C. Cattaneo, On the conduction of heat, Atti del Seminario Matematico e Fisico dell'Universitá di Modena 3 (3).
[9] C. Cattaneo, Sur une forme de l'équation de la chaleur éliminant le paradoxe d'une propagation instantanée, C.R. Acad. Sci. 247 (4) (1958) 431–433.
[10] P. Vernotte, Les paradoxes de la théorie continue de l'équation de la chaleur, C.R. Acad. Sci. 246 (22) (1958) 3154–3155.
[11] W. Dreyer, H. Struchtrup, Heat pulse experiments revisited, Continuum Mech. Thermodyn. 5 (1993) 3–50.
[12] M.N. Özisik, D.Y. Tzou, On the wave theory in heat conduction, ASME J. Heat Transf. 116 (1994) 535–536.
[13] D.S. Chandrasekharaiah, Hyperbolic thermoelasticity: a review of recent literature, Appl. Mech. Rev. 51 (12) (1998) 705–729.
[14] D.S. Chandrasekharaiah, Thermoelasticity with second sound: a review, Appl. Mech. Rev. 39 (3) (1986) 355–376.
[15] B.D. Coleman, W.J. Hrusa, D.R. Owen, Stability of equilibrium for a nonlinear hyperbolic system describing heat propagation by second sound in solids, Arch. Ration. Mech. Anal. 94 (3) (1986) 267–289.
[16] D.E. Glass, M.N. Özisik, D.S. McRae, B. Vick, On the numerical solution of hyperbolic heat conduction, Numer. Heat Transf. 8 (1985) 497–504.
[17] D.E. Glass, M.N. Özisik, D.S. McRae, Hyperbolic heat conduction with radiation in an absorbing and emitting medium, Numer. Heat Transf. 12 (1987) 321–333.
[18] L.H. Liu, H.P. Tan, T.W. Tong, Non-fourier effects on transient temperature response in semitransparent medium caused by laser pulse, Int. J. Heat Mass Transf. 44 (2001) 3335–3344.
[19] J. Zhang, J.J. Zhao, High accuracy stable numerical solution of 1D microscale heat transport equation, Technical Report 297-00, Department of Computer Science, University of Kentucky, Lexington, KY, 2000.
[20] J. Zhang, J.J. Zhao, Unconditionally stable finite difference scheme and iterative solution of 2D microscale heat transport equation, Technical Report 303-00, Department of Computer Science, University of Kentucky, Lexington, KY, 2000.
[21] J. Zhang, J.J. Zhao, Iterative solution and finite difference approximations to 3D microscale heat transport equation, Technical Report 320-01, Department of Computer Science, University of Kentucky, Lexington, KY, 2000.
[22] H.Q. Yang, Characteristics-based, high-order accurate and nonoscillatory numerical method for hyperbolic heat conduction, Numer. Heat Transf.: Part B – Fund. 18 (1990) 221–241.
[23] H.Q. Yang, Solution of two-dimensional hyperbolic heat conduction by high-resolution numerical methods, Numer. Heat Transf.: Part A – Appl. 21 (1992) 333–349.
[24] W. Shen, S. Han, Numerical solution of two-dimensional axisymmetric hyperbolic heat conduction, Comput. Mech. 29 (2002) 122–128.
[25] W. Shen, S. Han, A numerical solution of two-dimensional hyperbolic heat conduction with non-linear boundary conditions, Heat Mass Transf. 39 (2003) 499–507.
[26] J.B. Goodman, R.J. LeVeque, On the accuracy of stable schemes for 2D scalar conservation laws, Math. Comput. 45 (171) (1985) 15–21.
[27] R.J. LeVeque, Finite Volume Methods for Hyperbolic Problems, Cambridge texts in Applied Mathematics, Cambridge University Press, 2002.
[28] H.T. Chen, J.Y. Lin, Numerical analysis for hyperbolic heat conduction, Int. J. Heat Mass Transf. 36 (11) (1992) 2891–2898.
[29] H.T. Chen, J.Y. Lin, Analysis of two-dimensional hyperbolic heat conduction problems, Int. J. Heat Mass Transf. 37 (1) (1993) 153–164.
[30] G.F. Carey, M. Tsai, Hyperbolic heat transfer with reflection, Numer. Heat Transf. 5 (1982) 309–327.
[31] M.T. Manzari, M.T. Manzari, A mixed approach to finite element analysis of hyperbolic heat conduction problems, Int. J. Numer. Methods Heat Fluid Flow 8 (1) (1998) 83–96.
[32] M.T. Manzari, M.T. Manzari, On numerical solution of hyperbolic heat conduction, Commun. Numer. Methods Engrg. 15 (1999) 853–866.
[33] B.Q. Xu, Z.H. Shen, J. Lu, X.W. Ni, S.Y. Zhang, Numerical simulation of laser-induced transient temperature field in film-substrate system by finite element method, Int. J. Heat Mass Transf. 46 (2003) 4963–4968.
[34] X. Ai, B.Q. Li, A discontinuous finite element method for hyperbolic thermal wave problems, J. Engrg. Comput. 21 (5) (2004) 577–597.
[35] X. Ai, B.Q. Li, Numerical simulation of thermal wave propagation during laser processing of thin films, J. Electron. Mater. 34 (5) (2005) 583–591.
[36] W. Wu, X. Li, Application of the time discontinuous Galerkin finite element method to heat wave simulation, Int. J. Heat Mass Transf. 49 (2006) 1679–1684.
[37] X. Li, D.M. Yao, R.W. Lewis, A discontinuous Galerkin finite element method for dynamic and wave propagation problems in non-linear solids and saturated porous media, Int. J. Numer. Methods Engrg. 57 (2003) 1775–1800.

[38] P. Jamet, Galerkin-type approximations which are discontinuous in time for parabolic equations in a variable domain, SIAM J. Numer. Anal. 15 (5) (1978) 912–928.
[39] K. Eriksson, C. Johnson, S. Larsson, Adaptive finite element methods for parabolic problems, VI: analytic semigroups, SIAM J. Numer. Anal. 35 (4) (1998) 1315–1325.
[40] M.P. Zhang, C.W. Shu, An analysis of three different formulations of the discontinuous Galerkin method for diffusion equations, Math. Models Methods Appl. Sci. 13 (3) (2003) 395–413.
[41] O.C. Zienkiewicz, R.L. Taylor, S.J. Sherwin, J. Peiro, On discontinuous Galerkin methods, Int. J. Numer. Methods Engrg. 58 (8) (2003) 1119–1148.
[42] D.V. Kulkarni, D.V. Rovas, D.A. Tortorelli, Discontinuous Galerkin framework for adaptive solution of parabolic problems, Int. J. Numer. Methods Engrg. 70 (1) (2007) 1–24.
[43] K. Chrysafinos, N.J. Walkington, Error estimates for the discontinuous Galerkin methods for parabolic equations, SIAM J. Numer. Anal. 44 (1) (2006) 349–366.
[44] J. Palaniappan, S.T. Miller, R.B. Haber, Sub-cell shock capturing and spacetime interface tracking for nonlinear conservation laws, Int. J. Numer. Methods Fluids 57 (2008) 1115–1135, doi:10.1002/fld.1850.
[45] P.O. Persson, J. Peraire, Sub-cell shock capturing for discontinuous Galerkin methods, in: Proceedings of the 44th AIAA Aerospace Sciences Meeting and Exhibit, AIAA, Reno, NV, USA, 2006, pp. 5–18.
[46] R. Abedi, B. Petracovici, R.B. Haber, A spacetime discontinuous Galerkin method for elastodynamics with element-wise momentum balance, Comput. Methods Appl. Mech. Engrg. 195 (2006) 3247–3273.
[47] R. Abedi, S.-H. Chung, J. Erickson, Y. Fan, M. Garland, D. Guoy, R. Haber, J. Sullivan, S. Thite, Y. Zhou, Space-time meshing with adaptive refinement and coarsening, in: Proceedings 20th Annual ACM Symposium on Computational Geometry, 2004, pp. 300–309.
[48] R. Abedi, S.-H. Chung, M. Hawker, J. Palaniappan, S. Thite, R. Haber, Modeling evolving discontinuities with spacetime discontinuous Galerkin methods, in: A. Combescure, R. de Borst, T. Belytschko (Eds.), IUTAM Symposium on Discretization Methods for Evolving Discontinuities, vol. 5, Springer, 2007, pp. 59–87.
[49] M. Spivak, Calculus on Manifolds, W.A. Benjamin, Inc., New York, 1965.
[50] W.H. Fleming, Functions of Several Variables, Addison-Wesley, 1964.
[51] J. Palaniappan, R.B. Haber, R.L. Jerrard, A spacetime discontinuous Galerkin method for scalar conservation laws, Comput. Methods Appl. Mech. Engrg. 193 (2004) 3607–3631.
[52] J. Erickson, D. Guoy, J. Sullivan, A. Üngör, Building spacetime meshes over arbitrary spatial domains, in: Proceedings of the 11th International Meshing Roundtable (Sandia National Laboratories), 2002, pp. 391–402.
[53] A. Üngör, A. Sheffer, Pitching tents in spacetime: mesh generation for discontinuous Galerkin method, Int. J. Found. Comput. Sci. 13 (2) (2002) 201–221.
[54] J.R. Shewchuk, Triangle: engineering a 2D quality mesh generator and Delaunay triangulator, in: M.C. Lin, D. Manocha (Eds.), Applied Computational Geometry: Towards Geometric Engineering, Lecture Notes in Computer Science, vol. 1148, Springer-Verlag, Berlin, 1996, pp. 203–222.
[55] K.J. Baumeister, T.D. Hamill, Hyperbolic heat conduction equation – a solution for the semi-infinite body problem, ASME J. Heat Transf. 117 (1969) 256–263.
[56] D.Y. Tzou, Macro- to Microscale Heat Transfer, Taylor & Francis, 1997.
[57] Y. Zhou, M. Garland, R.B. Haber, Pixel-exact rendering of spacetime finite element solutions, Proc. IEEE Visual. 2004 (2004) 425–432.